RICE UNIVERSITY

Terahertz Absorption in Non-Polar Condensed Matter Systems

by

Jonathan Patrick Laib

A THESIS SUBMITTED
IN PARTIAL FULFILLMENT OF THE
REQUIREMENTS FOR THE DEGREE

Doctor of Philosophy

APPROVED, THESIS COMMITTEE:

R. Bruce Weisman (Chair)
Professor of Chemistry

Bruce R. Johnson
Distinguished Faculty Fellow in Chemistry

Daniel M. Mittleman
Professor of Electrical and Computer Engineering

HOUSTON, TEXAS
MAY 2010

ABSTRACT

Terahertz Absorption in Non-Polar Condensed Matter Systems

by

Jonathan Patrick Laib

Terahertz time-domain spectroscopy (THz-TDS) is a powerful non-contact optical technique for characterizing materials and sub-picosecond dynamic behavior in the far-infrared region (100 GHz – 10 THz) of the electromagnetic spectrum. As a young field (less than 25 years old), the terahertz spectral properties of many materials and physical processes remain unexplored. One of the most interesting, and fundamentally important, uncharacterized phenomena is the phase behavior of condensed matter systems. Normal (*n*)-alkanes are molecules of particular interest since they are linear, straight-chain hydrocarbons that are structurally simple and have melting points near room temperature. Using a custom designed spectrometer and sample cell, we characterize the terahertz optical properties of various liquid branched and *n*-alkanes (C_5H_{12} - $C_{16}H_{34}$) and use this as the basis to conduct imaging studies of a two-component surfactant/octane system to discern the content across the boundary layer. This prefaced our characterization of the phase behavior of longer *n*-alkanes where we observed novel temperature-dependent absorption features in the equilibrium non-liquid phases of *n*-tricosane ($C_{23}H_{48}$) through *n*-hexacosane ($C_{26}H_{54}$). These spectroscopic features have never previously been observed in non-polar (infrared inactive) materials, and provide new insight into the crystallization dynamics of organic molecular solids.

Acknowledgements

This thesis has been made possible through the selfless assistance and support of numerous people. First I want to thank my advisor, Dr. Daniel Mittleman, whose guidance and support brought this work to fruition and encouraged my own development as a scientist. These sentiments extend to the other members of my committee, Dr. Bruce Johnson and Dr. R. Bruce Weisman, whom I met as an undergraduate summer researcher and were instrumental in my decision to attend graduate school at Rice University. I want to thank Dr. Jason Deibel and Dr. Hui Zhan for teaching me everything I know about terahertz spectroscopy, and Daniel Nickel whose assistance made completing this work, and my graduation, possible. Over the years I worked with numerous members of the Mittleman Group who all deserve special thanks for their personal and professional contributions including Dr. Kanglin Wang, Dr. Zhongping Jian, Dr. Tushar Prasad, Dr. William Chan, Dr. Rajind Mendis, Dr. Joong-Wook Lee, Victoria Astley, Marx Mbonye, Jingbo Liu, and Ying Huang. I also want to thank all of the collaborators and staff that facilitated this work such as Dr. Jeremy Pearce, Dr. Reinaldo Navarrete, Paul Tortorici, Sue Friend, Sofia Medrano-Correa, Diana Warren, Vicki Schutter and especially Dwight Dear who helped me build all of the custom experimental equipment.

Personally, I want to thank my family, both immediate and extended, whose unwavering support made it possible for me to overcome the most difficult times in graduate school. Last, but not least, I want to thank my wife, Amity, who at great personal cost has been with me since the beginning and not only is solely responsible for my graduation but also gave me the greatest gifts in my life.

Contents

Illustrations

Chapter 1

Introduction

1.1 Terahertz Spectroscopy

Terahertz (THz) radiation can be found between the microwave and far-infrared regions of the electromagnetic spectrum and is named after its characteristic frequency, 1 THz or 10^{12} Hz, which defines its period (1 ps), wavelength (300 μm), wave-number (33 cm^{-1}) and energy (4.1 meV). The THz band encompasses a broad spectral range from approximately 100 GHz to 10 THz and bridges the gap between the optical and microwave regimes to marry many of the technologies otherwise segregated to either the long or short wavelength ends of the spectrum. Prior to 25 years ago, there were few reliable sources of THz radiation so it is a young field with numerous physical systems and molecules yet to be characterized. Practically, most non-conducting media are transparent to THz radiation and almost all chemical and biological molecules have unique THz spectral signatures. These features, combined with the ability to resolve sub-picosecond (ps) dynamics, make the THz band one of the most versatile regions of the electromagnetic spectrum.

While far-infrared frequencies have been used to conduct spectroscopy since the 1890s [1], the first concerted sub-millimeter (THz) pulses weren't generated until the advent of ultrafast lasers in the 1970s. Using ps pulses, spectrally narrow (bandwidth limited) radiation at the foot of the THz region was generated via optical rectification (difference frequency mixing) in a non-linear $LiNbO_3$ crystal [2]. With the invention and refinement of femtosecond (fs) dye lasers [3, 4], the first, and still most widely used, broadband THz sources were developed in the late-1980s in the form of optoelectronic

switches (photoconductive antennas) [5, 6]. Coherent coupling of generation and detection methods, either another time-gated switch or electro-optic sampling [7], forms the basis for the most prominent spectroscopic technique labeled terahertz time-domain spectroscopy (THz-TDS). This technique is predicated upon the use of ultrafast (< 100 fs) laser pulses to generate and detect single-cycle electromagnetic (THz) pulses. Doing this coherently allows direct measurement of the electric field of the THz pulses in the time domain, which upon Fourier transformation into the frequency domain, yields both the spectral amplitude and phase over the entire bandwidth of the pulse. This distinguishes THz-TDS from most traditional spectroscopic techniques that only measure the intensity and thus provide an incomplete description of a system's optical properties. The discovery of fs pulse generation from solid-state Ti:Sapphire lasers [8], proved to be the breakthrough for the field as their high power and small temporal pulse widths dramatically increased the signal and bandwidth of THz spectrometers while simultaneously decreasing their complexity, size, and cost. Subsequently, there was an explosion in the number of scientists specializing in THz research developing novel experiments and applications.

Initial research focused on characterizing the spectra of small molecules and gases which exhibit resonant rotational and ro-vibrational transitions in the THz region [9, 10]. Spectroscopic analysis quickly expanded to liquids [11-13], solids [14-16], biological molecules [17-20], explosives [21, 22] and various unique applications such as μL chemical component identification [23] and in-situ flame analysis [24] which are only possible with THz spectroscopy. This was followed by the development of time-resolved, pump-probe techniques which can characterize transient charge mobility [25],

conductivity [26, 27], carrier relaxation dynamics [28], and charge transport mechanisms [29] occurring on sub-ps time scales.

In addition to spectroscopy, imaging has emerged as a large field of study. Due to the wavelength and contrasting absorption properties in various materials, THz radiation can yield sub-mm resolution images containing greater information (spectral amplitude and phase) than traditional optical imaging techniques [30]. Imaging applications include quality control [31], defect analysis [32], security screening [33] and potentially medical diagnostic imaging through the development of multi-dimensional imaging techniques [34].

The feasibility of practical spectroscopic and imaging applications dramatically increased with the introduction of commercially available plug-and-play THz-TDS systems as expert technicians are no longer required to align, maintain, and operate complex equipment. Now cost-effective THz spectrometers can be installed to operate in nearly any conditions to achieve a variety of objectives (i.e. high signal, large bandwidth, high sample throughput) and require minimal computational effort to produce real-time results. In the end, all of these characteristics combined with its optical and spectroscopic properties and low energy, make THz spectroscopy a powerful non-contact, non-ionizing and non-destructive analytical tool.

1.2 Scope of this Thesis

My doctoral research has focused on developing novel experimental equipment and techniques to conduct temperature-dependent spectroscopic studies on the phase behavior of non-polar condensed matter systems. This thesis outlines the details of all

the custom instrumentation developed with that goal in mind, and the results obtained from the studies conducted.

In Chapter 2, I will describe the propagation of far-infrared radiation in condensed matter and review the previous condensed matter studies performed using THz spectroscopy. This will include both polar and non-polar molecules characterized in liquid and solid states and lead into a discussion of the difficulties encountered by theoreticians attempting to model the experimentally observed spectra (particularly of weakly bound solids). Additionally, the lack of phase transition studies in the THz region will be discussed, and our rationale for focusing on *n*-alkanes to begin condensed matter experiments.

In Chapter 3, I will introduce terahertz time-domain spectroscopy and discuss the most prominent THz generation and detection techniques. This will preface the details of the custom transmission THz-TDS we built with a particular emphasis placed on maximizing the bandwidth and signal-to-noise (S/N) ratio of the system. To conduct temperature-dependent phase transition experiments, we built a custom transmission cell capable of precisely controlling the temperature of our samples and with a path length tailored to preserve the high frequency components of the bandwidth as the transition is made from the liquid (transparent) to the solid (dispersive) states.

Chapter 4 will describe our studies of liquid condensed matter systems. I will begin with our characterization of the THz optical properties of all the *n*-alkanes that are liquid at 25°C and various branched isomers to correlate the spectral profiles with their physical properties. Extending upon our liquid work, we use a commercial THz-TDS system (Picometrix's T-Ray 4000) to perform THz imaging studies on a two-component

surfactant/octane system to quantify the variation of the chemical composition across the micro-emulsion phase boundary.

Chapter 5 will describe our work studying the unique phase behavior of *n*-alkanes which possess a distinct intermediate phase between the liquid and solid states known as the rotator phase. The stability of the rotator phase is influenced by chain-length and dictates whether the liquid-solid phase transition is either first or higher (continuous) order. For chains with 22 or fewer carbon atoms, the rotator phase is transient or metastable leading to first order phase transitions, while higher order phase transitions occur for chains with 23 or more carbon atoms and have fully stable rotator phases. Using our custom THz-TDS system and temperature-controlled sample cell we characterize the phase transitions of *n*-hexadecane ($C_{16}H_{34}$) through *n*-hexacosane ($C_{26}H_{54}$) and observe clear spectroscopic signatures of the first and higher order phase transitions. For *n*-docosane ($C_{22}H_{46}$) and smaller chains, no unique spectroscopic signatures emerge across the phase states as the spectral profiles simply scale with the density changes associated with their first order phase transitions. However, in stable rotator phase *n*-alkanes (*n*-tricosane, $C_{23}H_{48}$, and larger) we observe an initial first order phase transition as a surface frozen monolayer condenses into steady-state equilibrium with the bulk liquid prior to the entire material undergoing higher order phase transitions into the rotator and solid phases.

In conclusion, Chapter 6 will summarize the work in this thesis and outline the potential for future research.

Chapter 2

Background

Condensed matter physics, most generally defined, focuses on studying the macro- and microscopic physical properties of non-gaseous matter. Since condensed matter physics incorporates the behavior of all liquid and solid matter, it is the largest area of research involving every scientific discipline (physics, chemistry, materials science, etc.). Liquids and solids are aggregated together, and distinguished from gases as condensed matter, principally due to their multiple order of magnitude difference in density. This macroscopic property and its variation across condensed and non-condensed phase states is a consequence of the physics at the microscopic level. More precisely, materials condense out of the sparse gaseous phase by reaching a more energetically and entropically preferred configuration where short-range attractive forces exceed that of the thermal and kinetic energy (at a specific temperature or pressure) to accumulate into much denser, more highly ordered (in the case of solids) phases [35].

Spectroscopy of condensed matter aims to understand the interaction of light with strongly interacting, correlated many body systems. Given the wide range of condensed matter, it is an almost infinitely broad topic with limitless materials to study (crystalline and non-crystalline solids, liquids, dielectrics, metals, soft condensed matter, etc.). For long wavelength (300 μm) and low energy (4.1 meV) THz radiation, condensed matter primarily yield broad "continuum" spectra, with resonances emerging through the the interaction with permanent or induced electric dipoles (stipulated by traditional spectroscopic selection rules). The lack of a molecular dipole in non-polar condensed matter, however, does not preclude the emergence of THz spectral features as the long-

range, low-frequency collective motions resonant with THz pulses can produce spectroscopic absorptions. Ultimately, the molecular composition (polar or non-polar) and phase state (liquid or solid) determines the nature of the condensed matter dynamics which are a consequence of the physics of the propagation of far-infrared (THz) radiation in the medium.

2.1 Propagation of Far-Infrared Radiation

The general wave-equation governing the time-dependent propagation of an electric field ($\hat{E}$) in a medium can be derived by separating the field variables in the original Maxwell's equations to yield (for a non-magnetic medium) [36]:

$$\nabla^2 \hat{E} = \varepsilon_r \varepsilon_0 \mu_r \mu_0 \frac{\partial^2 \hat{E}}{\partial t^2} + \mu_r \mu_0 \sigma \frac{\partial \hat{E}}{\partial t}, \tag{2-1}$$

where ε_r and μ_r are the permittivity and permeability of the medium, ε_0 and μ_0 are the permittivity and permeability of a vacuum and σ is the conductivity of the medium. The terms on the right hand side of the equation represent the displacement and conduction currents responsible for propagation in a medium and are utilized or ignored depending on whether the medium is a dielectric or metal. In the case of a purely dielectric medium ($\sigma = 0$), propagation along the z-direction can be described by simplifying equation 2-1:

$$\frac{\partial^2 \hat{E}}{\partial z^2} = \frac{\varepsilon_r}{c^2} \frac{\partial \hat{E}}{\partial t^2}. \tag{2-2}$$

One solution to this differential equation is:

$$\hat{E}(z) = E_0 \cos(2\pi n\nu x), \tag{2-3}$$

which describes the propagation of a plane wave in a lossless medium with refractive index, n. Practically, there are no lossless media so the electric field amplitude decays as a function of the propagation distance in the material specified by the Beer-Lambert Law:

$$\hat{E}(z) = E_0 Exp(-\frac{1}{2}\alpha z). \tag{2-4}$$

Equating the complex version of equation 2-3 with equation 2-4 yields:

$$\hat{E}(z) = E_0 Exp(2\pi i n\nu z), \tag{2-5}$$

containing the complex refractive index, ñ, defined as:

$$\tilde{n} = n - i\alpha/4\pi\nu = n - ik, \tag{2-6}$$

incorporating real (dispersive) and imaginary (absorbing; $k = \alpha/4\pi\nu$) components. By converting to angular frequency ($2\pi\nu = \omega$) equation 2-6 can be used to define the complex dielectric function ($\varepsilon(\omega)$):

$$\varepsilon(\omega) = \varepsilon'(\omega) - i\varepsilon''(\omega); \text{ and,} \tag{2-7}$$

$$\varepsilon'(\omega) = n^2(\omega) - k^2(\omega); \text{ and,} \tag{2-8}$$

$$\varepsilon''(\omega) = 2n(\omega)k(\omega), \tag{2-9}$$

which describes a systems' response to an applied electric field (permittivity). More importantly, by characterizing the frequency-dependent absorption coefficient ($\alpha(\omega)$) and refractive index ($n(\omega)$) all of a materials' optical properties can be completely determined since the complex dielectric function directly relates to the susceptibility, conductivity or any other polarization (electrically correlated, collective response) of a material. The complex dielectric function provides such a versatile theoretical foundation that it can be adapted to quantitatively describe the dynamic behavior of all condensed matter systems (liquid and solid) with the nature of the collective response dictated primarily by the composition of the system (i.e. electric dipoles).

2.2 Liquid Phase Terahertz Studies

2.2.1 Polar Liquids

In polar liquids, THz radiation is largely absorbed due to the various interactions with electric dipoles, which in bulk media exhibit dispersive and resonant regimes segregated at roughly 6 THz [11]. At lower frequencies the material response to THz pulses is overdamped and diffusive (non-resonant) as the slowly varying electric field aligns the molecular dipoles and then they collectively reorient. This correlated process decays exponentially through collision induced relaxation and can be modeled using analytic expressions that relate the frequency-dependence of the complex dielectric function to the bulk reorientational intermolecular dynamics. The most widely applied treatment is the Debye model which provides relaxation times (τ_D) for the bulk reorientation [37]:

$$\varepsilon(\omega) = \varepsilon(\infty) + \frac{\varepsilon_0 - \varepsilon(\infty)}{1 - i\omega\tau_D}, \tag{2-10}$$

where ε_0 and $\varepsilon(\infty)$ are the static and high-frequency permittivity. This model can describe single and multiple relaxation processes or incorporate numerous modifications (Cole-Cole, Cole-Davidson, Havriliak-Negami) to extend its applicability to any liquid or soft-condensed matter system as a function of diverse variables (temperature, composition, etc.) [38-41]. Using THz-TDS a wide range of polar liquids have been characterized to study their solvation dynamics [42-45], often using small path-length reflection configurations due to the high absorption of the polar molecules ($1/\alpha$ = skin depth). The most widely studied polar solvent is water [46-48] where it's been determined that three Debye relaxation processes are present [49]. At large frequencies (>6 THz) the material response to THz pulses becomes resonant and spectral features arise as periodic librations or translations within a solvent cage produce absorption bands that deviate from the dielectric relaxation models [50].

2.2.2 Non-Polar Liquids

There is at least 60 years of far-infrared studies of non-polar liquids using sub-millimeter and microwave spectroscopy [51-56]. These techniques typically only characterize the absorption coefficient by measuring the modulation of transmitted light. Due to this limitation determining the complex dielectric function was only possible through difficult Kramers-Kronig analysis. However, by using THz-TDS the characterization is straightforward and numerous transmission studies have been conducted [57-60]. While the absence of electric dipoles dramatically reduces the absorption by non-polar liquids, transiently induced dipoles produced by collisions can cause far-infrared spectral features to emerge. In the 1950s, a spectroscopist named Poley observed a discrepancy between the experimentally measured spectral profiles and

the theoretical Debye model even when accounting for the Debye plateau in non-polar liquids (Figure 2-1) [61].

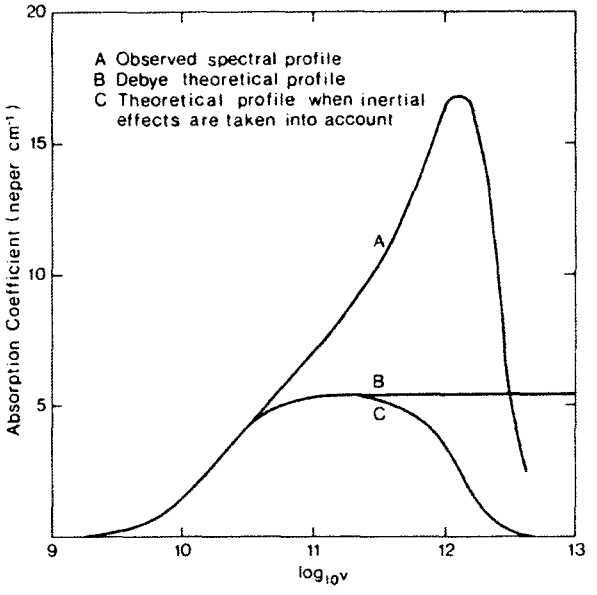

Figure 2-1: The experimentally observed and theoretically calculated absorption profiles for chlorobenzene featuring the Poley absorption peak (A-C).

This additional absorption is known as the Poley absorption band and is attributed to vibrations of the "liquid-lattice" corresponding to a smeared out lattice vibrational spectrum [62]. For non-polar liquids there is no Debye relaxation process so only the Poley peak is observed. To extract information from the absorption, a model for predicting and fitting the absorption profile of non-polar liquids was introduced in the form of the generalized Langevin equation [63]:

$$\alpha(\omega) = \frac{\varepsilon_0 - \varepsilon(\infty)}{nc}\omega^2 \,\mathrm{Re}\{C(i\omega)\} = \frac{\varepsilon_0 - \varepsilon(\infty)}{nc}\omega^2 \frac{\gamma K_0 K_1}{\gamma^2(K_0 - \omega^2)^2 + \omega^2(\omega^2 - K_0 - K_1)^2} \quad (2\text{-}11)$$

This model utilizes a generalized, truncated memory function to yield a parametric equation (Equation 2-11) that relates the Fourier transform of the correlation function, $C(i\omega)$, to a parametric equation that is completely phenomenological and makes no assumptions about the system it is applied to. Despite its generalized nature it connects the absorption coefficient to the correlation decay of the rotationally induced dipole through the extraction of time constants from γ. Furthermore, it treats K_0 and K_1 as fitting parameters that are ensemble averages of all the molecular interactions, although the interpretation of their origin is still unclear. Of the four parameters present in the generalized Langevin equation, K_0 is of particular interest because it can be related to $2k_BT/I_c$, where I_c is the moment of inertia about the symmetry axis.

2.3 Solid Phase Terahertz Studies

Of all the condensed matter spectroscopic work conducted with THz-TDS, the vast majority has focused on solid-state materials, specifically semiconductors. This is a consequence of the unique absorptions observed in their spectral profiles related to either lattice modes (phonons) [16, 64] and intraband transitions [65] or various dynamic charge carrier processes (conductivity, mobility, etc.) [66-68]. To quantify the transport properties of free carriers in solids, the Drude model of electrical conduction is typically invoked and is mathematically equivalent to the Debye model in liquids. The Drude model relates directly to the complex dielectric function to yield relaxation times (τ) for the charge carriers [69], and quantify the frequency-dependent ($\sigma(\omega)$) and static (σ_0) conductivity:

$$\varepsilon(\omega) = \varepsilon_0 + i\frac{\sigma(\omega)}{\omega}\text{; and,} \qquad (2\text{-}12)$$

$$\sigma(\omega) = \frac{\sigma_0}{1 - i\omega\tau}. \tag{2-13}$$

For most intrinsic semiconductors, the relaxation time of the free carriers is the sole parameter governing the frequency-dependent optical properties and occur on a time scale (1 ps) corresponding to the THz frequency range. Using THz-TDS the effects of dopants or other carrier traps on the dynamics can be determined in both static [70, 71] and transient [72, 73] studies. Beyond semiconductors, THz-TDS has also been used to characterize polymers [74, 75], insulators [76, 77] and superconductors [78, 79].

In addition to THz-TDS transmission studies, direct THz emission is another technique for characterizing the photophysics of semiconductors. Direct THz emission requires high mobility semiconductors capable of accelerating photogenerated charge carriers over short time scales (1 ps) in the presence of a large intrinsic or applied electric field. I will discuss the current surge mechanism further in Chapter 3. The in-situ generation of THz pulses provides a powerful experimental approach for investigating transient photoconductive properties of materials since the spectral emission profile is directly determined by the carrier mobility and recombination rates. To date, this has been predominantly achieved in inorganic semiconductors [80-82], although there has been some recent success with organic semi-conducting polymers [83, 84].

A more recently pursued avenue of condensed matter THz research is the spectroscopic characterization of solid-state organic and biological molecules. The spectra of these molecules differ from other condensed matter in that they display rich and distinct resonant absorption features attributed to long-range, low-frequency vibrational motions. These modes are a product of global inter- and intra-molecular

interactions involving every atom in the molecule resulting from unique molecule specific 'skeletal' motions that are extremely sensitive to environmental conditions. Investigations have been conducted studying DNA [85, 86], sugars [87, 88], amino acids [89], polypeptides [90], explosives [21, 22, 91], illicit drugs [33, 92, 93], pharmaceutical compounds [94, 95], structural polymorphs [96, 97] and the effects of hydration [98, 99]. The emergence of specific resonant absorption features forces the abandonment of the traditional analytical models used to fit dispersive dielectric relaxation. In their place, more rigorous theoretical approaches are applied that begin scaling with the $3N - 6$ normal modes (N is the number of atoms) and account for the forces at work including the dominant intramolecular modes that are modified by the weaker intermolecular interactions such as van der Waals forces and hydrogen bonding. Overall, modeling and assigning the THz spectra of solid-state biological molecules is a many-body problem involving numerous weak collective interactions that are not well characterized either experimentally or theoretically. While theoretical modeling has been performed successfully on biological systems [100-102], extending it further requires the determination of a wide variety of weakly correlated inter- and intramolecular potentials. It is with this goal in mind that the *n*-alkanes are interesting.

2.4 normal-(*n*)-alkanes

Normal-(*n*)-alkanes are linear, straight-chain hydrocarbons that contain only single bonds and are governed by the generic structural formula: C_nH_{2n+2} [103]. Since *n*-alkanes are non-polar and involve no hydrogen bonding, they present the simplest condensed matter systems to study with melting points near room temperature. Chemically, *n*-alkanes are the fundamental component of "soft" materials (all non-solid

condensed matter) which include surfactants, liquid crystals, biological membranes and lipids. For many of these materials, their chemical and biological utility is dictated by the physics of their phase behavior which, in turn, is dominated by the hydrocarbon component. Although the *n*-alkanes are structurally simple, this simplicity does not translate through to their phase behavior.

If any physical property is plotted as a function of temperature, the traditional first order phase behavior is not displayed by *n*-alkanes as they are cooled through their melting point. Instead a divergence emerges where chains with 22 carbon atoms or less undergo first order transitions, while those with 23 carbon atoms or more undergo a higher (continuous) order transition (with multiple first order phase transitions) denoted in figure 2-2 by the roll-over in the increase of the density as a function decreasing temperature [104].

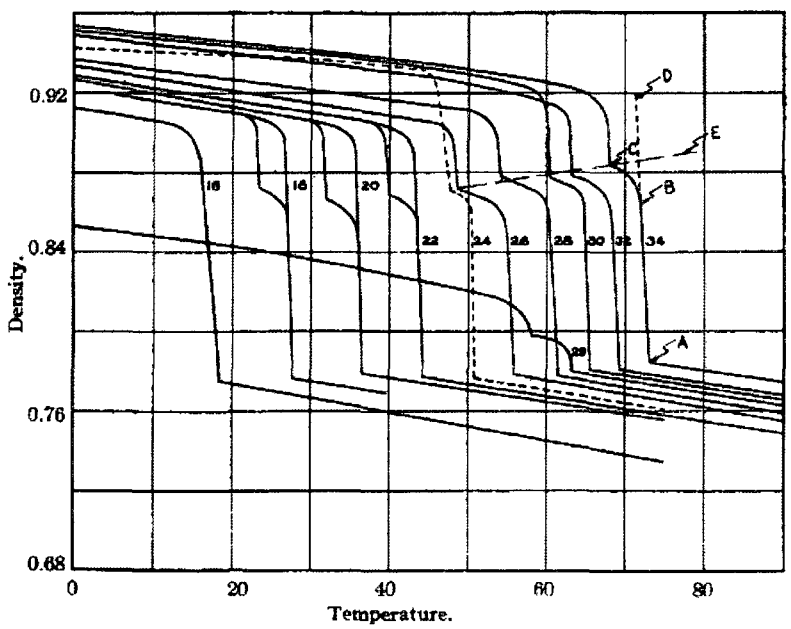

Figure 2-2: Plot of density vs. temperature for even *n*-alkane chain lengths from *n*=16-34.

This behavior is attributed to the presence of a distinct intermediate phase between the liquid and solid states known as the rotator phase [105, 106]. In the *n*-alkanes, the stability (and thus the order of the phase transition) is dictated by chain length so that chains with less than 23 carbon atoms have a metastable or transient rotator phase while those with at least 23 carbon atoms have a fully stable rotator phase [107-110]. On a molecular level, the crystallization dynamics proceed along the pathway illustrated in Figure 2-3 whereby the completely disordered liquid state condenses into the fully ordered crystal state through the rotator phase. The rotator phase incorporates elements of both phases in the form of short-range disorder embedded within a larger long-range structural order. This creates a "quasi" liquid often referred to as the plastic phase.

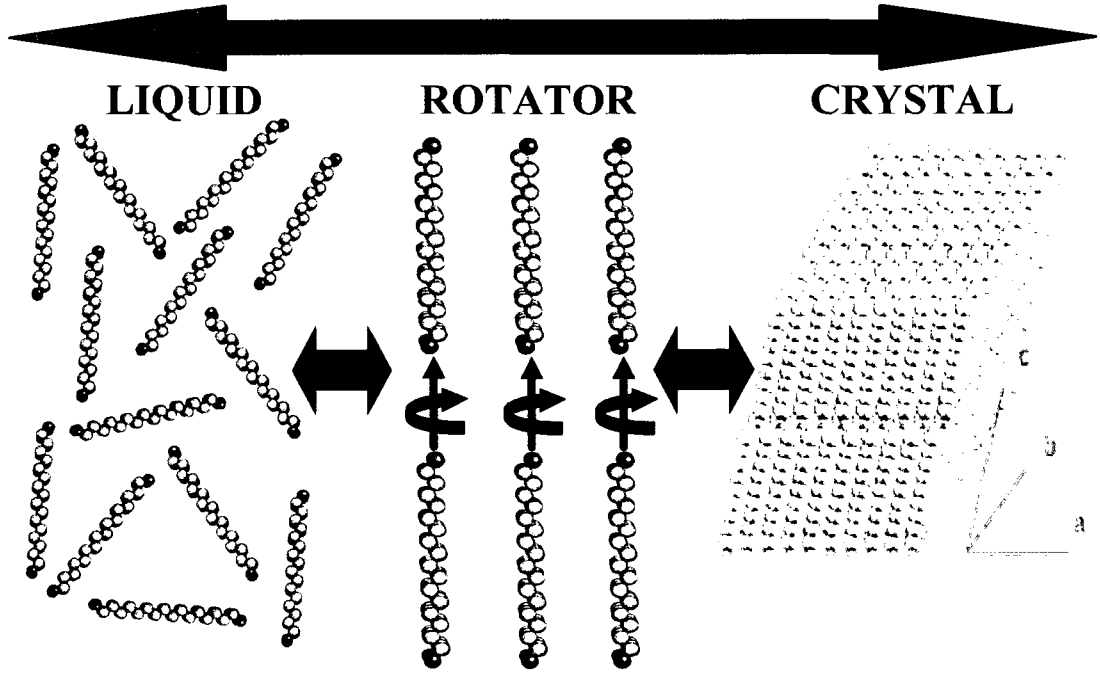

Figure 2-3: Crystallization pathway in *n*-alkanes.

In addition to the orientational disorder present along the longitudinal axis, there is also the presence of conformational disorder due to kinking along the chains (Figure 2-4) [111].

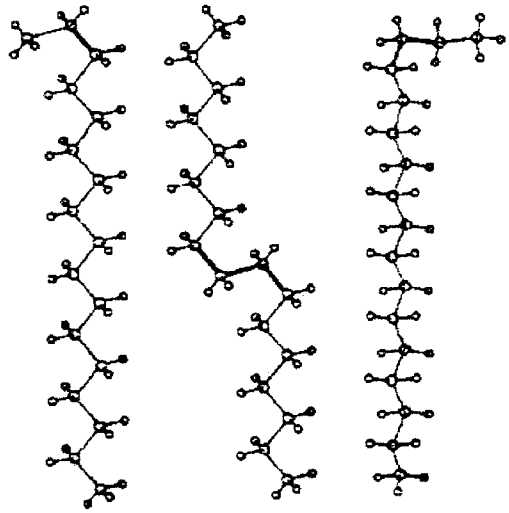

Figure 2-4: Conformational disorder present in *n*-alkanes due to kinking along the chains.

Despite the interesting phase behavior present in *n*-alkanes, they have almost never been studied using THz-TDS and there is only a single example of a polymer being characterized through its' phase transition [112]. The main reason for this is the assumption that these non-polar (infrared inactive) materials lack informative spectral features. Additionally, the absence of far-infrared optical properties across the condensed phases requires extensive preliminary spectroscopic characterization to inform the design of custom experimental equipment capable of obtaining temperature-dependent spectral profiles. Filling the void in the THz spectrum makes studying the *n*-alkanes and their phase transitions worthwhile, even in the absence of resonant spectral features. Ultimately, characterizing the phase behavior of *n*-alkanes as a function of both chain-

length and temperature would provide an understanding of the most elementary molecular systems (weakly bound van der Waals crystals). More importantly, the *n*-alkanes would serve as scaffolding capable of systematic functionalization along their carbon backbone to quantify inter- and intra-molecular interactions and inform ongoing theoretical work.

Chapter 3

Terahertz Time-Domain Spectroscopy

As mentioned previously, while what is now known as the terahertz band has been coincidentally probed for over 80 years using far-infrared and sub-millimeter spectroscopy [1, 51-56], it wasn't until the introduction of the fs pulsed laser that the THz region of the electromagnetic spectrum became truly accessible. This was a direct outgrowth of research dealing with the propagation of transient signals along transmission lines [5, 6]. The discovery that the transients were far-infrared radiation that could be generated, propagated through free space and detected provided all the elements of a spectrometer to form the basis for terahertz time-domain spectroscopy (THz-TDS). The technique derives its name from the fact that the electric field of the radiation is mapped in the time-domain to yield both the spectral amplitude and phase of the pulses upon Fourier transformation into the frequency-domain (Figure 3-1).

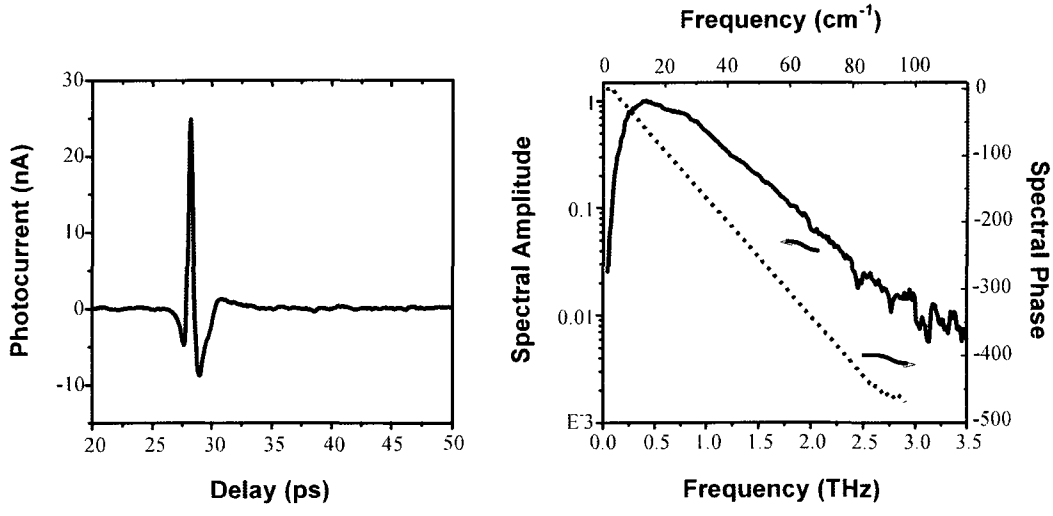

Figure 3-1: THz waveform (left) and Fourier transformation (right) into the frequency-domain.

This provides a pulsed, spectrally broad, far-infrared probe able to completely characterize all optical properties that is insensitive to ambient background radiation as a result of coherent generation and detection of the pulses. Although the THz pulses in THz-TDS are temporally narrow it is not a time-resolved technique as only equilibrium properties are measured. While time-resolved studies have been developed to probe sub-ps dynamics, those are beyond the scope of this thesis and can be readily found in the literature [113, 114].

When it comes to the practical design and construction of a terahertz time-domain spectrometer, there are a select number of options available for generating and detecting THz radiation that are usually dictated by the ultrafast oscillator available and the desired operational objectives.

3.1 Terahertz Generation

To generate terahertz pulses for large bandwidth applications, there are two primary techniques used; optical rectification and optoelectronic switches (photoconductive antennas). Both techniques require ultrafast fs laser pulses to generate broadband terahertz radiation via second order non-linear processes; however, the differences in the mechanisms result in different performance characteristics.

3.1.1 Optical Rectification

Optical rectification is the difference frequency generation of all the frequency components present in a spectrally broad (temporally narrow) optical pulse (Figure 3-2). In a non-centrosymmetric medium, the non-linear polarization (P) created by the presence of an intense electric field (E) can be written as:

$$P(\omega) = \varepsilon_0 \chi^{(2)}(\omega = \omega_1 - \omega_2) | \mathrm{E}(\omega) |^2, \tag{3-1}$$

where ε_0 is the permittivity of free space and $\chi^{(2)}$ is the second order susceptibility tensor.

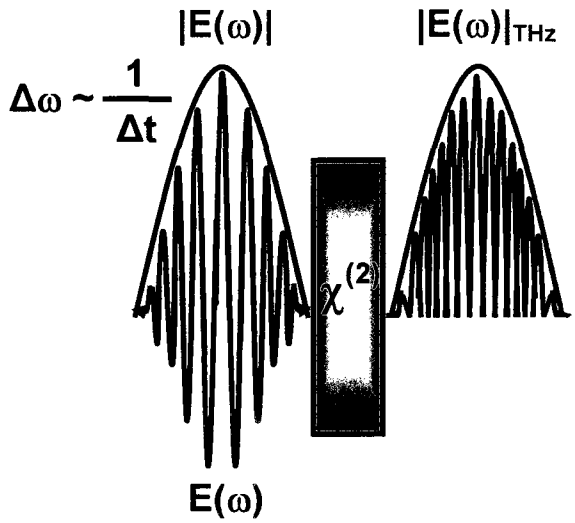

Figure 3-2: Optical rectification from a non-linear medium

Fourier transformation of $P(\omega)$ yields the time-dependent polarization, $P(t)$, and when a fs optical pulse is used a THz pulse is emitted [115]:

$$E(t)_{THz} \sim \frac{\partial^2 P}{\partial t^2}. \tag{3-2}$$

It is labeled rectification because the rapid oscillations of the electric field are "rectified" so that only the envelope of the polarization transient remains, which is composed of the weighted sum of all the difference frequency contributions. As a second order non-linear process, optical rectification is proportional to the second order susceptibility of the

optical medium and has exceptionally low conversion efficiency (~10^{-6}-10^{-7}). However, it does yield enormous spectral bandwidth as a consequence of being directly proportional to the inverse of the narrow fs optical pulse duration [116, 117].

3.1.2 Photoconductive Antenna

The second, and most widely used, technique to generate terahertz pulses involves photoconductive (PC) antennas. These devices are based on a current-surge mechanism governed by Faraday's law of induction (Maxwell's equations):

$$E(t)_{THz} \sim \frac{\partial J}{\partial t}. \tag{3-3}$$

This equation states that a time-varying electric current (accelerating charge) will radiate an electromagnetic pulse which is the mechanism responsible for the generation of all electromagnetic waves found in nature. PC antennas consist of a high mobility semiconductor (~10^3 cm^2/Vs) with a band gap matched or exceeded by the energy of the incident optical pulses (typically $\geq$1 eV). On the semiconductor surface a conductive electrode gap is deposited which is connected to a DC bias voltage. The electrode gap and voltage are flexible to be set over a wide range of values so long as they combine to provide an electric field on the order of ~10^3 V/cm. When a band-gap tuned, ultrafast optical pulse is directed between the electrodes of the antenna, charge carriers are promoted from the valence band to the conduction band and accelerate to the oppositely charged electrode due to the presence of the large electric field. These accelerated charges radiate an electromagnetic pulse perpendicular to the electrode gap in a

characteristic dipole radiation pattern that can be collimated using a hemispherical dome lens (Figure 3-3) [6].

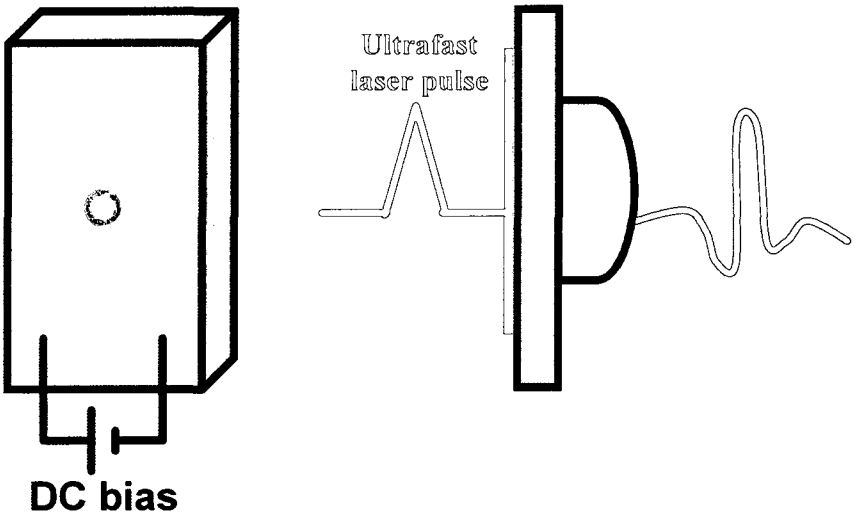

Figure 3-3: Photoconductive antenna (left) in a THz transmitter (right).

To generate terahertz frequency (10^{12} Hz) radiation the charge carriers must be created and accelerated on a sub-ps time scale, thus explaining the need for fs lasers. Ultimately, even though photoconductive antennas are based upon a second order non-linear process, like optical rectification, their dependence on charge generation, and acceleration, dramatically increases the conversion efficiency approaching 0.2%.

3.2 Terahertz Detection

To detect terahertz pulses, the two techniques used are simply derivatives of the second order non-linear generation methods.

3.2.1 Photoconductive Antenna

Just as photoconductive antennas are the predominantly used method for generating THz pulses, they also are the most widely employed detection technique. To

be used as a detector, the physical configuration is identical to a transmitter except that rather than applying a DC bias voltage across the electrode gap, one is provided by the THz electric field. By time-gating the detector synchronously in the presence of the THz electric field, the photogenerated charge carriers are free to oscillate across the surface of the detector and generate an electric current whose amplitude and sign are directly proportional to those of the incident THz field (again dictated by Faraday's law of induction; Figure 3-4).

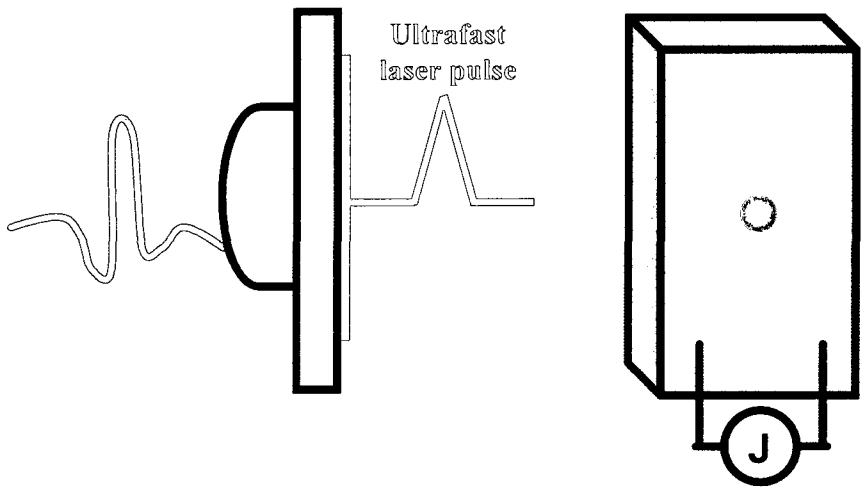

Figure 3-4: A THz receiver (left) using a photoconductive antenna (right).

Coherent time-gating of the emitter and detector allows the electric field to be mapped with a current detector in the time-domain by simply stepping a variable delay line.

3.2.2 Electro-Optic Sampling (EOS)

The second detection technique is electro-optic sampling (EOS), which is the inverse of the second order non-linear phenomena responsible for optical rectification. It is based on the Pockels effect where an applied voltage can induce a birefringence in a non-linear medium. In this detection setup (Figure 3-5) the terahertz radiation co-

propagates with a linearly polarized probe beam through an electro-optic crystal. The electric field of the coincident THz pulse modifies the index ellipsoid of the detector crystal which modulates the phase of the probe beam by rotating the polarization.

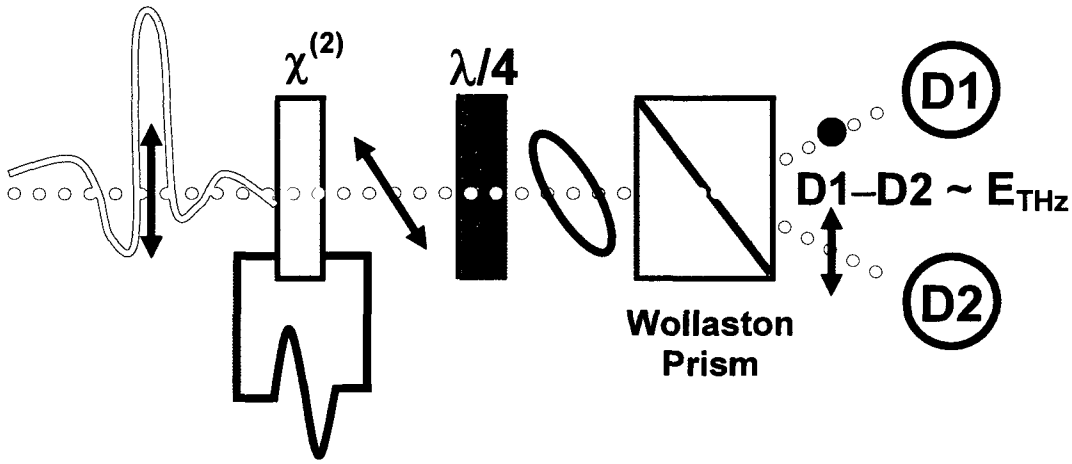

Figure 3-5: An electro-optic sampling (EOS) detection setup

This phase change can be converted into an intensity change through the use of cross polarization optics (a $\lambda/4$ plate followed by a Wollaston prism) to produce an elliptically polarized beam whose orthogonal components can be separated and measured using a balanced photodetector. The difference between the detectors is directly proportional to the THz electric field (E_{THz}) which is directly proportional to the phase delay (Γ) induced in the probe beam. This is described by:

$$\Gamma = \frac{\pi d n^3 \gamma_{41}}{\lambda} E_{THz}, \tag{3-4}$$

where d is the thickness of the electro-optic crystal, n is the refractive index at the wavelength of the probe beam, λ is the probe wavelength, and γ_{41} is the electro-optic coefficient [7].

3.3 Generation and Detection in Concert

Utilizing generation and detection techniques in a THz-TDS system requires certain practical considerations dictated by the ultrafast oscillator and the desired operational objectives. While each of the generation and detection schemes is interchangeable, certain combinations can be selected to satisfy experimental demands. For instance, to obtain the highest possible signal, a photoconductive transmitter and receiver will typically be paired together because they provide the highest possible optical-to-THz signal conversion efficiency. In commercially available fiber-coupled THz-TDS systems, signal-to-noise (S/N) ratios of up to 80 dB can be achieved with 100 Hz scan rates using PC antennas and high speed scanning delay lines. Generating such a large signal is accomplished at the expense of the bandwidth as even the fastest excitation and recombination semiconductors still frequency limit the resonant behavior of the fundamental dipole structure. For this reason, paired photoconductive switches typically obtain less than 2 THz bandwidth, depending on the temporal width and alignment of the pulses used to time-gate the antennas.

Conversely, if the objective is to achieve the highest possible bandwidth, optical rectification paired with electro-optic sampling can exceed 100 THz bandwidth [118]. This too is achieved at a cost, as thin electro-optic crystals (~150 μm) must be employed to minimize dispersion and preserve the high frequency signal components (via phase matching). The reduction in the interaction length of the THz pulses reduces the

birefringence they induce in the electro-optic crystal thereby reducing the signal. This can be compensated for by employing amplified ultrafast oscillators, with dramatic improvements in signal achieved recently with novel oscillators [119, 120]; however, this incurs increasing cost and complexity. Ultimately, the combination of emitter and detector pair chosen for a terahertz time-domain spectrometer can be selected to achieve any operational objective, high signal and bandwidth or rapid collection rates and are versatile enough to operate in almost any environment or experimental configuration (transmission, reflection, attenuated total reflection), depending on the optical density of the materials being studied.

3.4 Large Signal and Bandwidth Terahertz Time-Domain Spectrometer

Given the unamplified Ti:Sapphire oscillator available for our THz-TDS system, and the goal of obtaining both high signal and large bandwidth to conduct transmission spectroscopy, we decided to employ a photoconductive antenna as the THz generator and EOS as the detector in our custom THz-TDS system (Figure 3-6) [121]. In our THz-TDS system, we utilize a Coherent MIRA mode-locked Ti:Sapphire ultrafast laser with a repetition rate of 76 MHz and a steady-state output power of 800 mW wavelength tuned to 780 nm. The pulsed output was chirped by the output coupler resulting in a temporal width of ~100 fs (see Figure A-1 in the Appendix). To achieve the broadest possible spectral bandwidth in the frequency-domain, we had to minimize our gate pulses in the time-domain so we installed an external group velocity dispersion (GVD) compensator (a pair of prisms) to compress the temporal pulse to the smallest possible width (80 fs; see Figure A-2 in the Appendix). The dispersion compensated pulse is split into two beams, one to gate the THz emitter and the other to be used as the linear probe beam for our EOS

detection setup. To optimize both the signal and bandwidth generated from our THz source, we chose to build a custom THz emitter using semi-insulating (SI) GaAs as the semiconductor in the PC antenna.

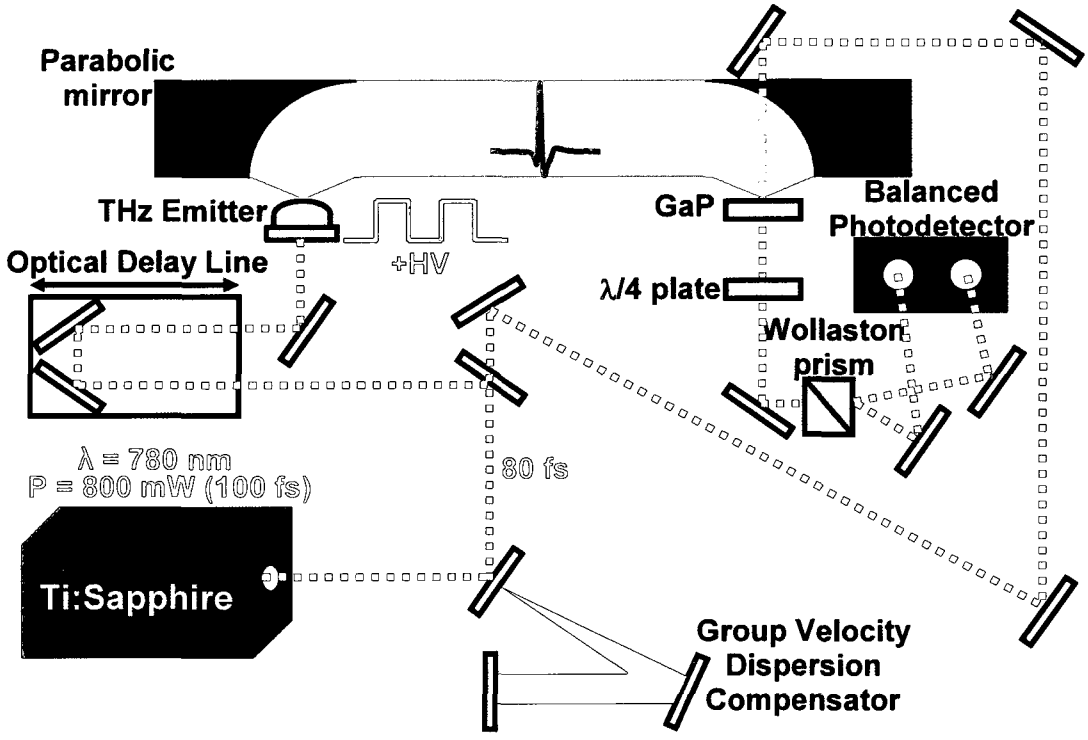

Figure 3-6: Schematic of the custom THz-TDS we built.

This was done because SI-GaAs provides an optimal combination of large charge mobility (8000 cm^2/Vs) and short carrier lifetimes (τ_c ~100 ps) conducive to large bandwidth generation [122]. As a χ^2 process, the THz signal generated from a PC antenna scales as a second order function with respect to the optical power applied, so to maximize the signal we needed to apply the largest optical power possible. This meant reducing the number of optical components in the system to apply a large, unfocused

beam (~500 μm beam diameter) on the antenna, which dictated the spacing of the electrodes on the antennas surface (Figure 3-7).

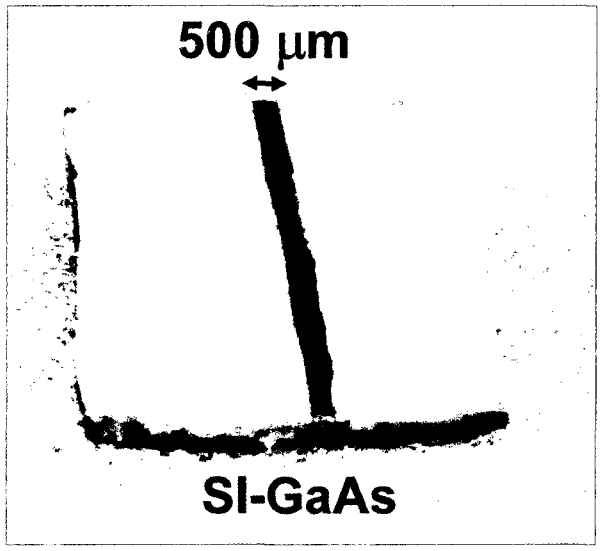

Figure 3-7: A 8.035 mm x 8.035 mm x 0.63 mm thick SI-GaAs wafer (dimensions dictated by the collimating lens dimensions) with a 500 μm electrode gap silver painted on the surface.

A 500 μm electrode gap can be applied using silver paint, thus avoiding the time and effort normally associated with photolithographically depositing small aperture spaced electrodes (~50 μm apart). The spacing dictates the use of a large voltage (~1000 V) to achieve the requisite field strength necessary to accelerate the photogenerated charge carriers and emit THz pulses. Despite using a large voltage, SI-GaAs PC antenna as our THz emitter, the signal is weak and necessitates the use of lock-in amplification to demodulate and filter the THz signal from the noise background. This means incorporating a reference modulation signal usually supplied by a mechanical optical chopper. Optical choppers, though, dramatically reduce the optical power (50% reduction typically) and can only achieve sub-kHz modulation frequencies which defines the noise level obtained through an inverse ($1/f$) relationship. To avoid these

limitations we built a high voltage square-wave generator using a transistor switch (Figure 3-8).

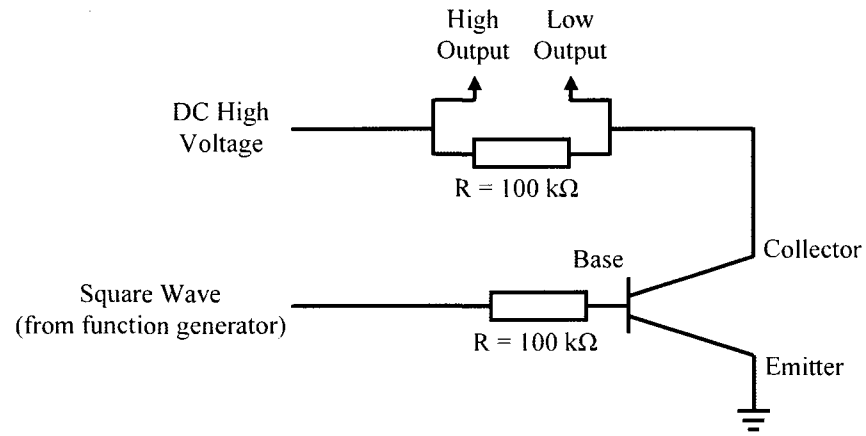

Figure 3-8: Transistor switch design for HV square wave generator (NPN power transistor).

Using this circuit we could apply a 1000 V, 5 kHz (order of magnitude larger) reference modulation signal and ~175 mW of optical power to the THz emitter. The combined high optical and electrical power required the fabrication of a custom mount that could be actively cooled to dissipate the heat generated on the emitter, which would otherwise impair the photophysics of the semiconductor in the PC antenna. This necessitated the use of a thermally conductive, electrically insulating and mechanically robust material for the mount, for which there are not widely available economical options. Fortunately, one was found in the form of Corian, which is a synthetic composite made by DuPont that is most frequently used as a kitchen counter-top material. Because of this, free samples were obtained and machined to the appropriate dimensions and the SI-GaAs wafer with silver painted electrodes could be mounted using conductive epoxy and connected to our circuit. To cool the emitter, quick-connect valves were run through the Corian and connected to a water circulator, with the finished emitter shown below (Figure 3-9)

including a hemispeherical lens glued on to collimate the generated THz radiation [123]. Due to how sensitive the THz signal is to the input optical power (a χ^2 process), maintenance of a consistent beam alignment on the electrode gap is the most significant variable in achieving a stable signal. To this end, we installed a commercial laser beam stabilization system (BeamLock 4D purchased from TEM Messtechnik GmbH) that uses a position sensitive detector connected through a feedback loop to piezoelectric actuators on 2 different mirrors immediately after the GVD compensator. With this system the beam can be effectively stabilized through four degrees of freedom (two beam positions and two angles) at the emitter (and detector) so that the THz signal varies in direct proportion (as the square) to only the laser power which was monitored and recorded for all of the measurements.

To detect the signal, we chose to use an EOS detection setup with a 300 μm thick <110> GaP electro-optic detector crystal (<110> specifies the crystal orientation using Miller indices). This thickness was chosen to maximize both the bandwidth and signal as a thinner crystal would achieve higher bandwidth at the expense of the signal while also convolving reflections into the main pulse. Even the 300 μm thickness yields an internal reflection roughly 10 ps from the main pulse that was partially delayed by attaching a 500 μm thick <100> GaP crystal. The <100> orientation dictates a null transverse electro-optic effect and subsequent windowing of the reflections during signal processing serves to filter out all of the potential artificial frequency components.

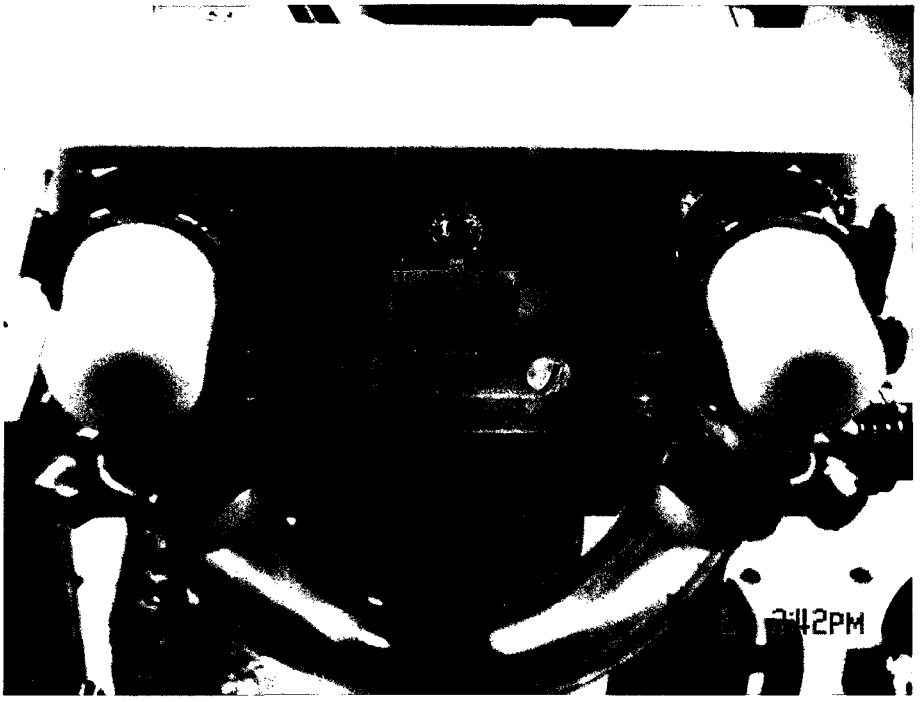

Figure 3-9: THz emitter installed in custom mount.

The interior of the finished spectrometer is shown in Figure 3-10 (with superimposed THz and probe beam paths) using collimating parabolic mirrors to minimize high frequency signal loss at unnecessary optical surfaces and is purged with dry nitrogen to remove strongly absorbing water vapor. The signal obtained from our spectrometer (Figure 3-11) has a S/N of 60 dB and a bandwidth of 3 THz which is an excellent blend of both high signal and large bandwidth, especially given the temporal width of the gate pulses (80 fs).

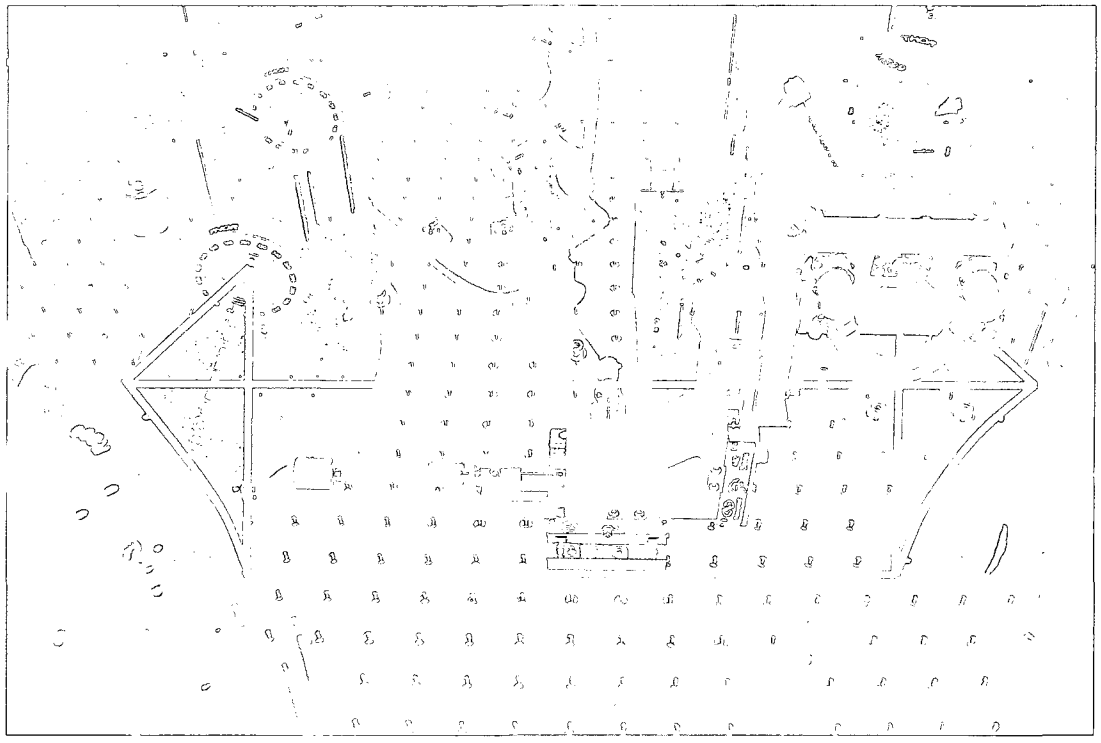

Figure 3-10: Spectrometer internal configuration with THz (green) and probe beam (red) paths.

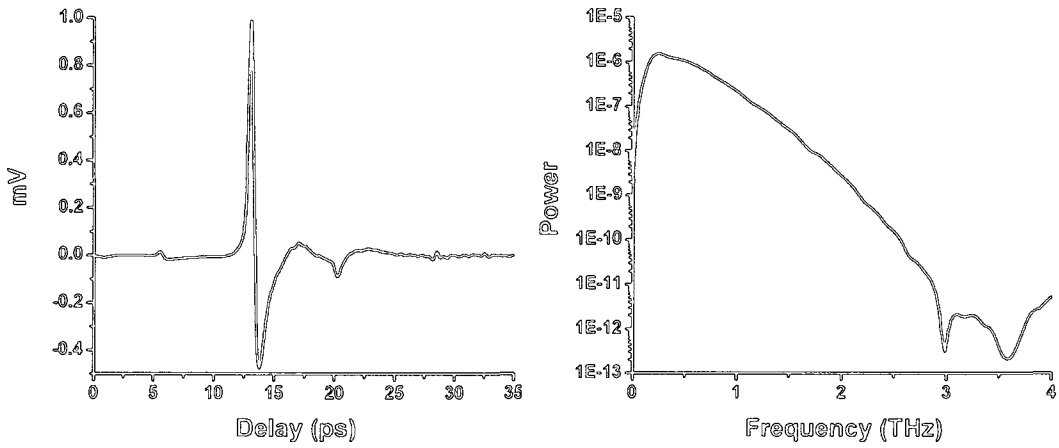

Figure 3-11: THz waveform (left) and FFT (right) from our custom THz-TDS system.

3.5 Temperature-Controlled Transmission Sample Cell

To characterize the THz spectral properties of non-polar, *n*-alkane phase transitions, which are weakly absorbing (infrared inactive), a chemically inert transmission sample cell capable of precise temperature control was required. Given these specifications, and the unique internal dimensions of our spectrometer, we decided to design and build one ourselves. Our sample cell (Figure 3-12) is composed entirely out of stainless steel with the exception of the z-cut, single crystal quartz windows (THz transparent) and the PTFE (Teflon) o-rings used to seal them.

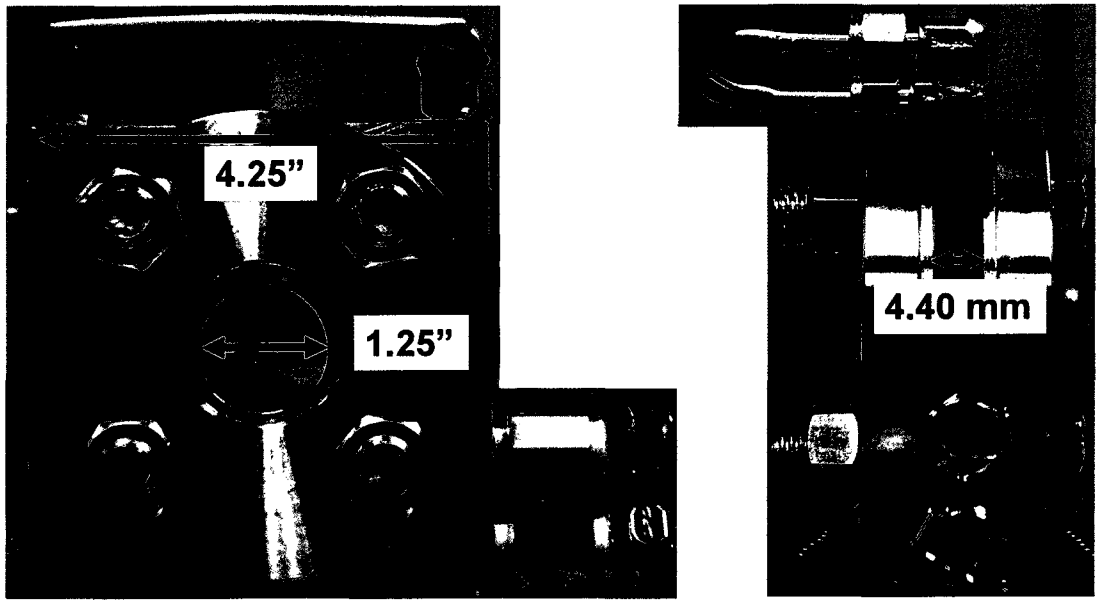

Figure 3-12: Temperature-controlled transmission sample cell

Using stainless steel ensures that the cell is chemically inert and also provides the best possible heat capacity and thermal conductivity for our thermal reservoir. Due to the incompressibility of the solid phases we aimed to study, we had to use a fixed path cell and settled on the smallest internal path length that could seal using o-rings: 4.40 ± 0.05 mm. To control the temperature, internal fluid lines were drilled in the body of the cell

that connected to a water circulator capable of heating and cooling the cell from 0°C to 80°C in 0.1°C increments. While the diameter of the cell windows is smaller than the diameter of the THz beam (~3", dictated by the diameter of the parabolic mirrors), a 1" aperture was installed prior to the cell to screen the outer fringes of the beam that contain the low frequency components of our signal with the highest S/N. The signal was sacrificed to minimize the amount of material used in the cell and better control its temperature and phase behavior.

3.6 Material Parameter Extraction from a Single Path Length Cell

In a traditional Beer-Lambert's Law experimental scenario, a sample cell is filled with a sample and then the path length is varied with measurements made at each path length. Using THz-TDS, where the electric field is measured, the material parameters, $\alpha(\omega)$ and $n(\omega)$, can be calculated using the following equations [124]:

$$n(\omega) = \frac{-\phi c_0}{\omega d} + 1 \text{ ; and,} \tag{3-5}$$

$$\alpha(\omega) = \frac{-2\ln[\rho]}{d}, \tag{3-6}$$

where c_0 is the speed of light in a vacuum, ϕ is the phase differences across the measurements, ρ is the ratio of the electric field amplitudes (E/E_0) across the measurements, ω is the angular frequency and d is the difference in the path lengths across the measurements. The use of multiple path lengths, each with the sample present, simplifies the calculation of the frequency dependent absorption coefficient as the

transmission coefficient across each optical surface is identical for each measurement and normalizes out in the ratio of the electric field amplitudes. This simplification does not persist upon reducing to a single path length cell experiment. While ϕ becomes the phase difference between the empty cell (reference) and the filled cell (sample), maintaining the formulation of equation 3-5 to calculate the refractive index, the calculation of the absorption coefficient must account for the transmission across the inhomogeneous optical surfaces between the reference and sample measurements. This is done by calculating the Fresnel transmission coefficients across each surface:

$$t_{12} = \frac{2n_1}{n_1 + n_2}. \tag{3-7}$$

In a single path length experiment, the transmission of the THz electric field through the empty cell reference can be described by the following equation:

$$E_0 = t_{air/win} Exp[-(\alpha d)/2] Exp[(i\omega n_{air} d)/c] t_{win/air}. \tag{3-8}$$

For transmission through the sample-filled cell, the THz electric field can be written as:

$$E_0 = t_{sam/win} Exp[-(\alpha d)/2] Exp[(i\omega n_{sam} d)/c] t_{win/sam}. \tag{3-9}$$

The ratio of the reference and sample waveforms (equations 3-8 and 3-9) can then be taken to compute the frequency-dependent absorption coefficient:

$$\alpha(\omega) = \frac{2}{d} \ln\left(\frac{n_{air}(n_{sam} + n_{win})^2}{n_{sam}(n_{air} + n_{win})^2} \frac{E}{E_0} \right). \tag{3-10}$$

Given the equations for calculating $\alpha(\omega)$ and $n(\omega)$, the accuracy of the measurements depends on the most uncertain dynamic parameters in the experimental setup; the path length and the THz signal due to fluctuations in the laser power. The uncertainty can be computed using partial derivatives:

$$\delta n = \delta n_d + \delta n_\phi, \tag{3-11}$$

$$\delta \alpha = \delta \alpha_d + \delta \alpha_\rho, \tag{3-12}$$

$$\delta n_d = \frac{\partial n}{\partial d} \delta n = \frac{\phi c_0}{\omega d^2} \delta d, \tag{3-13}$$

$$\delta n_\phi = \frac{\partial n}{\partial \phi} \delta \phi = -\frac{c_0}{\omega d} \delta \phi, \tag{3-14}$$

$$\delta \alpha_d = \frac{\partial \alpha}{\partial d} \delta d = \frac{2 \ln(\rho)}{d^2} \delta d \text{ ; and,} \tag{3-15}$$

$$\delta \alpha_\rho = \frac{\partial \alpha}{\partial \rho} \delta \rho = -\frac{2}{d} \frac{\delta \rho}{\rho}. \tag{3-16}$$

In our system the dominant noise is due to fluctuations of the THz signal caused by the variation in the laser power. This noise is multiplicative and thus the phase error is roughly equal in the sample and reference spectra:

$$\delta\phi_s \approx \delta\phi_r , \tag{3-17}$$

so that in the case of the phase difference, $\delta\phi = (\phi_s - \phi_r)$,

$$\delta\phi \approx 2\delta\phi_r . \tag{3-18}$$

The noise in the ratios of the reference and sample electric field amplitudes can be estimated by adding up the relative uncertainty from both the reference and sample:

$$\frac{\langle \delta\rho^2 \rangle}{\rho^2} = \frac{\langle \delta\rho_r{}^2 \rangle}{\rho_r{}^2} + \frac{\langle \delta\rho_s{}^2 \rangle}{\rho_s{}^2} . \tag{3-19}$$

Since the relative error is again roughly equal for the reference and sample:

$$\frac{\delta\rho}{\rho} \approx \sqrt{2}\,\frac{\delta\rho_r}{\rho_r} ; \text{ and,} \tag{3-20}$$

$$\delta\rho \approx \sqrt{2}Exp(-d\alpha/2)\frac{\delta\rho_r}{\rho_r} . \tag{3-21}$$

Plugging the Beer-Lambert's equations for $\alpha(\omega)$ and $n(\omega)$ (equations 3-5 and 3-6) into the relations for uncorrelated noise sources:

$$\langle n^2 \rangle = \langle n_a{}^2 \rangle + \langle n_\phi{}^2 \rangle ; \text{ and,} \tag{3-22}$$

$$\left\langle \delta\alpha^2 \right\rangle = \left\langle \delta\alpha_d{}^2 \right\rangle + \left\langle \delta\alpha_\rho{}^2 \right\rangle, \tag{3-23}$$

yields:

$$\delta n = \frac{n-1}{d}\left(\left(\frac{2c_0\delta\phi_r}{\omega(n-1)} \right)^2 + (\delta d)^2 \right)^{\frac{1}{2}} \text{; and,} \tag{3-24}$$

$$\delta\alpha = \frac{\alpha}{d}\left(\left(\frac{\sqrt{2}\delta\rho_r}{\alpha\rho_r} \right)^2 + (\delta d)^2 \right)^{\frac{1}{2}}. \tag{3-25}$$

For low absorbing measurements, dominated by noise associated with the THz beam, the error attributed to the path length can be ignored in equations 3-24 and 3-25 to give the following estimates for the noise in the refractive index and absorption coefficient:

$$\delta n = \frac{2c_0\delta\phi_r}{\omega d} \text{; and,} \tag{3-26}$$

$$\delta\alpha = \frac{\sqrt{2}\delta\rho_r}{d\rho_r}. \tag{3-27}$$

Chapter 4

Terahertz Spectroscopy of Liquid Condensed Matter Systems

4.1 Terahertz Optical Properties of Liquid *n*-alkanes

As mentioned previously in Chapter 2, while there have been numerous THz-TDS studies on non-polar liquids only a select few liquid *n*-alkanes have been characterized in the THz region [125]. To understand the condensed phase THz optical properties of *n*-alkanes, we began by using the aforementioned THz-TDS experimental setup and temperature-controlled sample cell (Chapter 3) to characterize, at 25°C and ambient pressure, all the chains that are liquid at room temperature (C_5H_{12} - $C_{16}H_{34}$). This experiment was conducted using samples obtained from a commercial vendor with purities in excess of 99.5%. The results are shown in Figure 4-1.

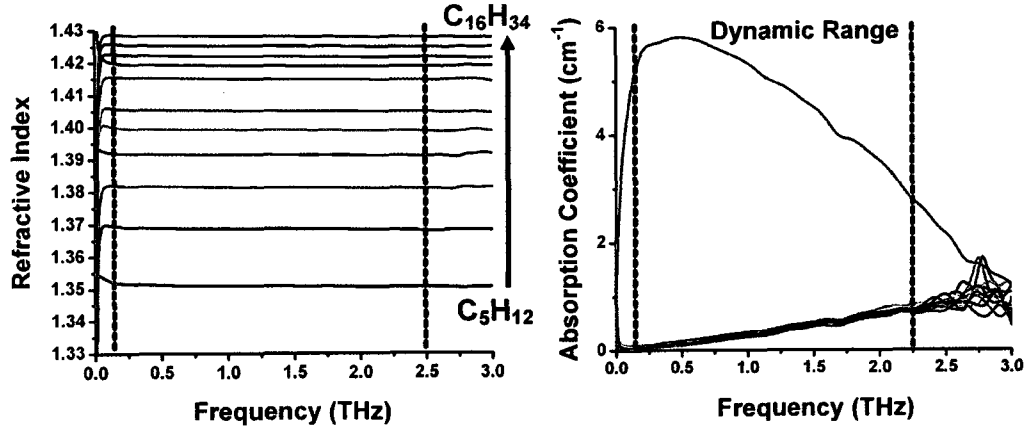

Figure 4-1: Frequency-dependent refractive indices, n(ω), and absorption coefficients, α(ω), of liquid C_5H_{12} - $C_{16}H_{34}$ at 25°C and ambient pressure. The dotted red lines indicate the effective bandwidth of each measurement, while the dynamic range specifies the maximum signal possible at each frequency component determined by dividing the reference spectrum by the noise floor.

When analyzing both plots it is immediately apparent that a relationship exists between the refractive index and chain length while none is present with respect to the absorption coefficient. Finding that the absorption coefficient is identical and small for the *n*-

alkanes (resulting from scattering) is not surprising given that each molecule lacks an appreciable dipole moment (<0.10 Debye [126]). To put this in perspective, the absorption coefficients are 3 orders of magnitude smaller than that of liquid water ($\alpha \sim$ 240 cm^{-1} at 1 THz [9]) which has a dipole moment of 1.6 Debye. Since the *n*-alkanes can only be differentiated by their refractive indices, it is instructive to use this material parameter to correlate with physical properties and identify potential relationships. The refractive index for each *n*-alkane (at 1 THz and optical frequency (Sodium D line)) can be found in Figure 4-2 and the first relationship examined is to carbon chain length since it is the only variable in the experiment (Figure 4-3).

n-alkane	*n* (1 THz) (± 0.001)	*n* (589.6 nm) (± 0.001)
n-pentane	1.351	1.358
n-hexane	1.369	1.375
n-heptane	1.382	1.387
n-octane	1.392	1.398
n-nonane	1.399	1.405
n-decane	1.405	1.411
n-undecane	1.410	1.417
n-dodecane	1.415	1.421
n-tridecane	1.419	1.425
n-tetradecane	1.422	1.429
n-pentadecane	1.425	1.431
n-hexadecane	1.428	1.434

Figure 4-2: Refractive indices of the *n*-alkanes at 1 THz and optical frequencies.

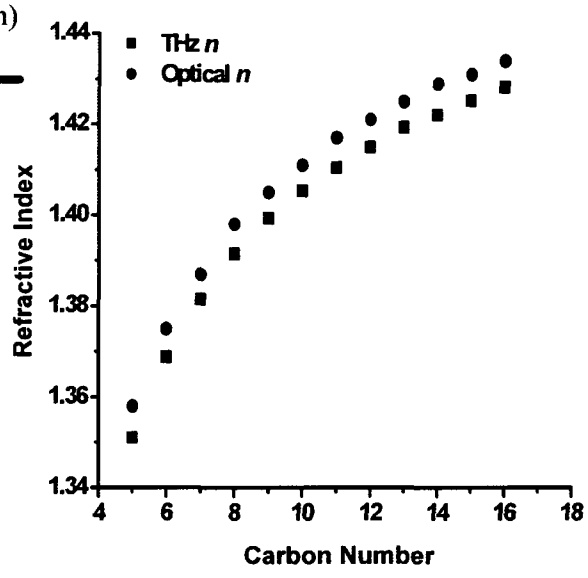

Figure 4-3: Carbon Number vs. Refractive Index.

Clearly, the THz and optical frequencies are very similar and scale identically in a non-linear manner as a function of carbon chain length. This relationship is not surprising since these molecules are bound strictly by van der Waals forces, specifically London

(dispersion) forces, governed by the interactions of higher multipoles that scale non-linearly as a function of chain length. Of greater interest is the relationship between the refractive indices and density depicted in Figure 4-4.

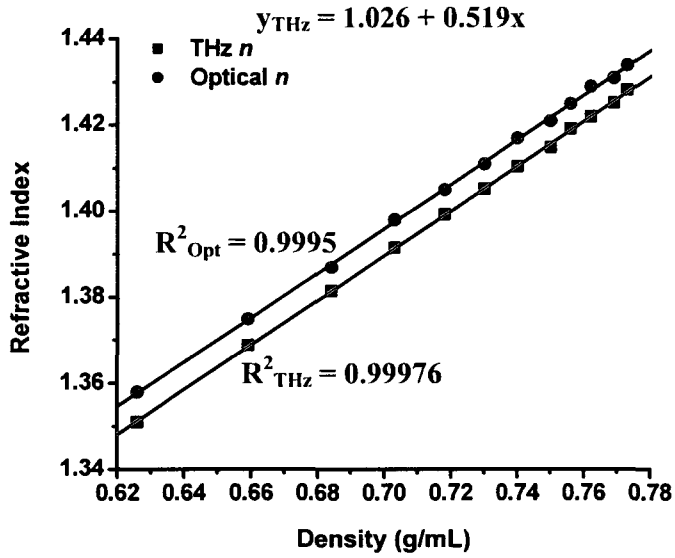

Figure 4-4: *n*-alkane Density vs. Refractive Index (at 1 THz and 589.6 nm).

The fact that both curves scale almost identically relative to the density of the *n*-alkanes indicates that material responses are identical for both regimes, and the almost perfect linear relationship ($R^2 > 0.999$) can be described by the Lorentz-Lorenz equation derived from dielectric theory (Equation 4-1) [127]:

$$\frac{n^2-1}{n^2+2} = \frac{N_A \alpha}{3M_w} \rho_m, \tag{4-1}$$

where ρ_m and M_w are the density and molecular weight of the material molecules, α is the mean molecular polarizability, and N_A is Avogadro's number. This equation can be

simplified into a direct linear relationship between n and ρ_m in the case of materials with small densities (non-solid condensed matter) where the molecules are far apart and weakly interacting so that the refractive index is close to 1. Under this condition, a Taylor expansion of the specific refraction at $n = 1$ gives:

$$\frac{n^2-1}{n^2+2} \approx \frac{2}{3}(n-1). \tag{4-2}$$

Using this approximation in equation 4-1 yields the following version of the Lorentz-Lorenz equation which linearly relates bulk macroscopic properties (refractive index) to microscopic origins (polarizability):

$$n = 1 + \frac{N_A \alpha}{2M_w} \rho_m. \tag{4-3}$$

Due to the assumptions made to derive this version of the Lorentz-Lorenz equation, it is restricted for use with only materials where $\rho_m < 1$, and the linear fit is valid for only homologous alkyl chains and the conditions under which they were characterized. The presence of molecular weight in the Lorentz-Lorenz equation enables the refractive index to be related to any physical properties dependent on that variable. For soft-condensed matter, surface tension (γ) and viscosity (η) can be associated with molecular weight through the following empirical relationships [128-130]:

$$\gamma \approx \frac{1}{M_w^{\ a}}; \text{ and,} \tag{4-4}$$

$$\eta \approx M_w^{\ b}. \tag{4-5}$$

The best correlations to the experimental data are obtained when the exponents a and b are set to 0.5 and 0.78 with the subsequent fits depicted in Figures 4-5 and 4-6.

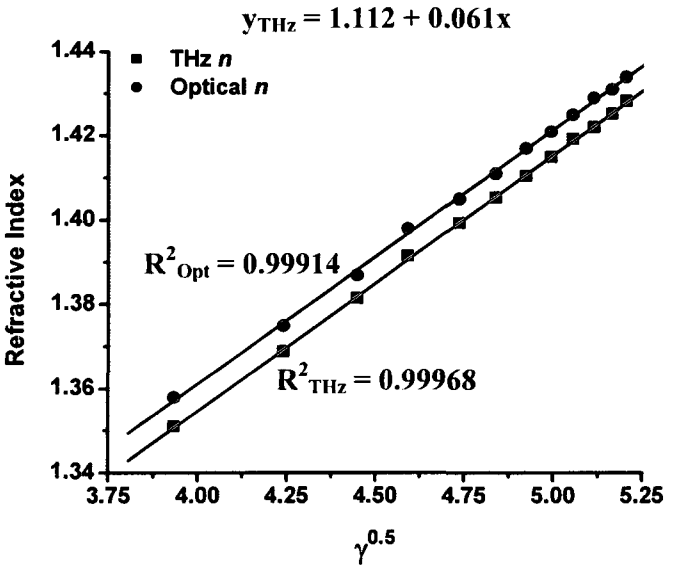

Figure 4-5: $\gamma^{0.5}$ (γ in mN/m) vs. Refractive Index (at 1 THz and 589.6 nm) for liquid *n*-alkanes.

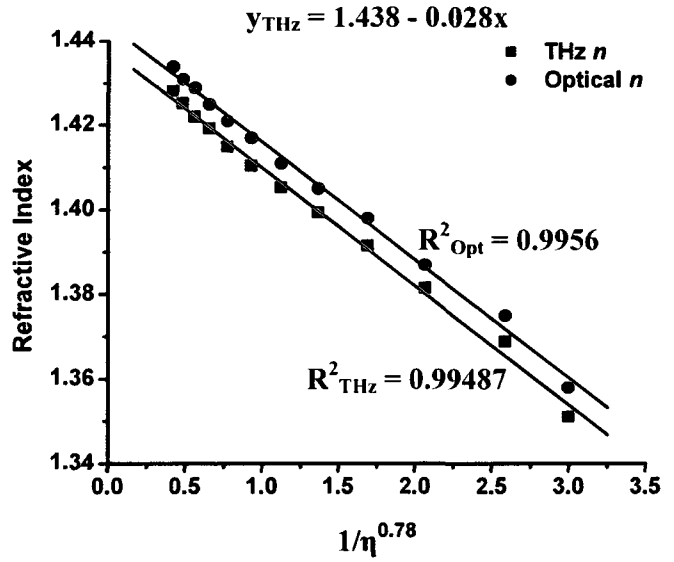

Figure 4-6: $1/\eta^{0.78}$ (η in mPa*s) vs. Refractive Index (at 1 THz and 589.6 nm) for liquid *n*-alkanes.

Both plots illustrate a high correlation between the refractive index and surface tension and viscosity, approaching that of density. Since the fits are tailored to the *n*-alkanes by fine-tuning the exponents in equations 4-2 and 4-3 empirically, they provide excellent calibration curves for determining unknown homologous alkane physical properties and distinguishing them from non-homologous alkyl-based systems (branched, aromatic, functionalized, etc.). This is a consequence of the inclusion of the mean polarizability in the slope of the fit (via the Lorentz-Lorenz equation) which is highly sensitive to conformational, polarity, and bonding variations. To qualitatively distinguish between linear and non-homologous alkanes, both the refractive index and physical property of a material are necessary to plot against a specific calibration curve. The ability to distinguish non-normal hydrocarbons is illustrated in Figure 4-7 using surface tension.

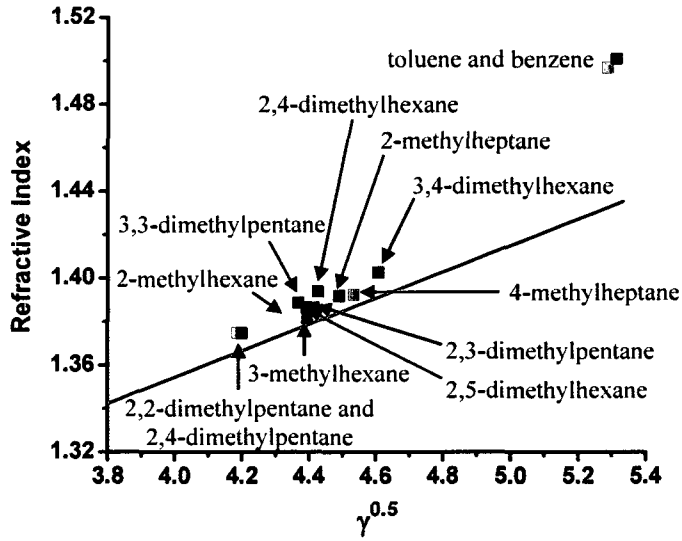

Figure 4-7: $\gamma^{0.5}$ (γ in mN/m) vs. Refractive Index for various branched and aromatic hydrocarbons relative to the calibration curve calculated from the *n*-alkane data at 25°C.

Ultimately, this represents an enormously powerful and straightforward qualitative tool capable of real-time analytical measurements for not only identifying *n*-alkanes, but also distinguishing them from non-homologous species. These calibration curves can be characterized across any variable (temperature, pressure, composition, etc.) to provide accurate methods for calculating unknown physical properties of large chain-length hydrocarbons that are otherwise difficult to experimentally determine. Furthermore, this method could be used to deduce the separate contributions to dispersion by various structural groups. While the optical and THz frequencies of the *n*-alkanes proved to be similar and scale almost identically relative to density, surface tension, and viscosity, frequency-dependent refractive indices are more readily determined with THz rather than optical pulses making it easier to apply this method at THz frequencies.

4.2 Terahertz Imaging of Alkyl Surfactants at Organic/Aqueous Interface

To extend from qualitative to quantitative analysis, discernible absorption coefficients are required to determine the concentrations of chemical components present in a system. For *n*-alkanes there are numerous practical systems where the interaction with polar species dictates the systemic behavior, preferentially or otherwise. The simplest such systems are aqueous surfactants. The word surfactant is an abbreviation of surface active agents which are compounds that are literally active at a surface and are distinguished by their ability to adsorb at interfaces [131]. An interface denotes a boundary between two immiscible phases and can exist between any combination of phases (solid-vapor, solid-liquid, liquid-vapor, etc.). Surfactants absorb at interfaces by reducing the surface tension to alter the interfacial free energies of the immiscible components. This is possible as a consequence of surfactants being amphiphilic,

possessing hydrophobic and hydrophilic groups, which makes them soluble in both organic and aqueous solvents at liquid-liquid interfaces. Aqueous surfaces at liquid-liquid interfaces are of particular interest as they dictate the fundamental molecular behavior in many physical, chemical, and biological processes such as membrane transport, protein folding, and micelle formation [132]. For the dynamics across bulk aqueous and hydrophobic solutions, the formation of micelles mediates the solvation of one component into the other.

Micelles are aggregates that can form in aqueous solution when the hydrophobic tails of a surfactant form a core encapsulating droplets of a non-polar liquid. The hydrophilic heads of surfactants are composed of ionic/polar functional groups and, through hydrogen bonding, disperse aggregates of otherwise insoluble liquids into aqueous solutions. Reverse micelles can be formed through the same process with surfactants instead assembling around polar molecules to disseminate them in non-polar media. Essentially surfactants act to kinetically stabilize mixtures between two immiscible liquids by creating emulsions whose behavior is governed through intermolecular hydrogen bonding between the hydrophilic groups and polar bulk solvent. As a result, surfactants can be broadly classified by the nature of the hydrophilic group into anionic, cationic, zwitterionic (dual charge) and nonionic species that can be varied to mediate between almost any immiscible components. Despite the widespread commercial and industrial application of surfactants, there are no high resolution methods for quantifying the variation of the components across the interfacial layer in-situ and only limited experimental studies of the dynamics been conducted [133-135]. These two

concerns make the characterization of surfactant induced emulsions between immiscible liquids a problem perfectly suited for examination by THz-TDS.

To quantify the components present across the interfacial layer and monitor their evolution as a function of time, rapid scan rates and high signal are needed to collect transmission spectra along a heterogeneous mixture involving a high absorbing aqueous phase. This necessitates the use of a commercial THz-TDS setup instead of our custom built large bandwidth spectrometer (Figure 4-8).

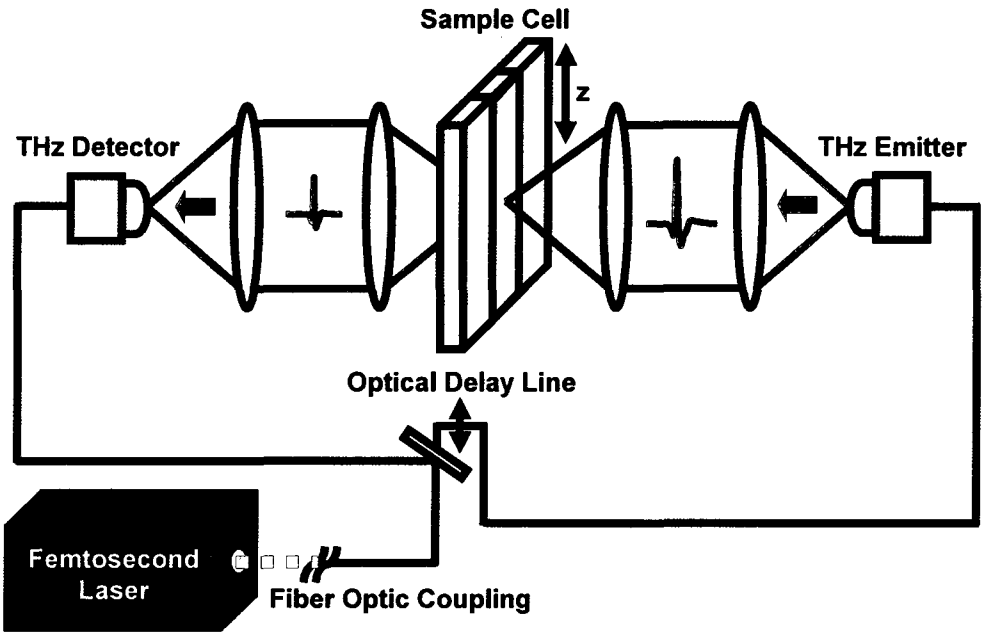

Figure 4-8: Schematic of experimental setup using a commercial THz-TDS setup.

The commercial instrument used is Picometrix's T-Ray 4000 which fiber-couples fs pulses to THz transmitters and receivers to achieve S/N ratios in excess of 70 dB with scan rates of 100 Hz. By using collimating lenses with focal lengths of 7.5 cm and focusing lenses with focal lengths of 3 cm, a frequency-dependent spot size of ~3 mm can be obtained which specifies the spatial resolution of the scans across the mixture.

Just as important as using a time-domain spectrometer with high signal and a rapid scan rate, is utilizing a transmission cell capable of chemically inert in-situ mixing that can be precisely translated through the THz beam. This required another custom built sample cell except this one is composed entirely out of single crystal quartz shown in Figure 4-9.

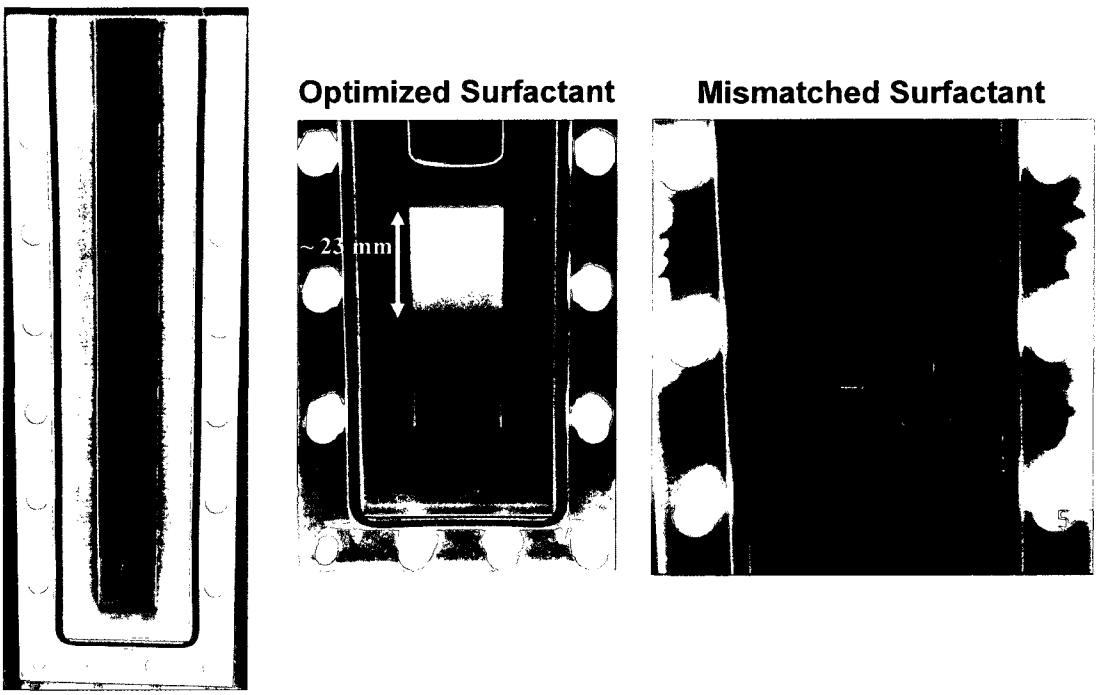

Figure 4-9: Single crystal quartz sample cell sealed with a nitrile corded o-ring and teflon screws and nuts (left). A microemulsion is created by an optimized surfactant mixed in-situ (center) and an immiscible interface is created by a mismatched surfactant (right).

To study the dynamic evolution of the interfacial layer, a model system was selected coupling *n*-octane with two different surfactants in 3% NaCl brine solution. The surfactants were selected to provide an optimized and mismatched component that preferentially emulsify the octane or leave the interface unaffected. Comparing the two systems would be the most useful test for determining whether THz-TDS can resolve the systemic differences that are illustrated visually in Figure 4-9. The optimized surfactant

is a cosurfactant consisting of an internal olefin sulfonate (RSO_2O^-) and an alkyl propoxy sulfate ($ROSO_3$) chosen specifically for their ability to preferentially emulsify octyl chains. This particular cosurfactant is so effective at emulsifying octane in aqueous brine that simple mixing is sufficient to create a macroscopically homogeneous, microscopically inhomogeneous layer between the two immiscible liquids known as a microemulsion. The intermediate microemulsion is a thermodynamically stable multi-component dispersion consisting of water, oil and surfactant with a sub-micron, heterogeneous structure that readily scatters light as demonstrated by the milky color of the interface illustrated in Figure 4-9. It is both the content and the evolution of this complex interface that we are interested in quantifying using THz-TDS. Unfortunately, while the internal path length of the cell was designed to be 1 mm, the manufacturer mistakenly built the cell with a 1.5 mm deep sample channel. This mistake prevents the transmission of any signal through the pure aqueous layer and restricts the ability to image across the boundary layer. Despite this, useful spectral information can still be extracted from the octane dominated areas of the interfacial layer.

The first experiment we performed using the sample cell was to determine the diameter of the THz beam by characterizing an immiscible mixture of water and *n*-octane. By translating across the interfacial boundary between the transparent *n*-octane and the opaque water we mimicked the technique used to characterize the diameter of optical beams with a dull knife-edge [136]. The result of the characterization is shown in Figure 4-10 with the normalized spectral amplitudes (selected at 200 GHz) plotted as a function of the distance along the two-component system. To estimate the spot size we fit the curve with a Boltzmann sigmoid function and then multiplied the distance between

the 20% and 80% values of the normalized full value of the curve by line shape parameters associated with Gaussian beam shapes (an realistic approximation for the THz beam shape). This method predicts a beam diameter of 2.31 ± 0.03 mm at 200 GHz. To estimate the error we calculated the standard deviation of the beam diameter acquired from multiple measurements of the stable water/octane system over a period of 4 hours.

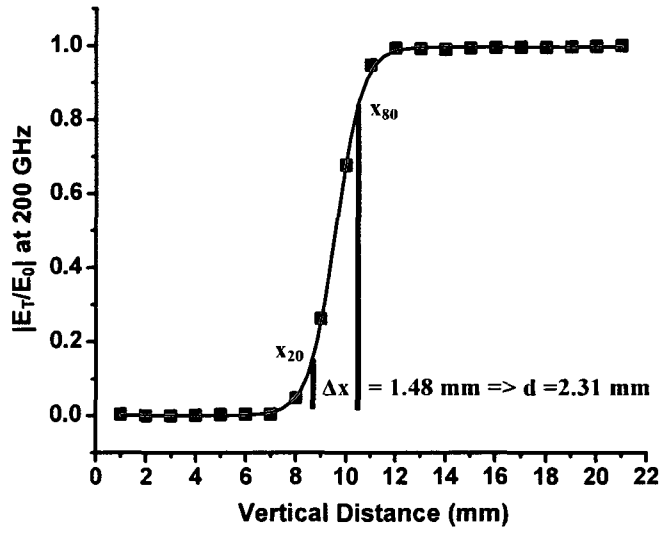

Figure 4-10: Normalized spectral amplitude (selected at 200 GHz) versus distance along the sample cell containing *n*-octane and water. This plot was used to estimate the beam size (imaging resolution) of our experiment.

In Figure 4-11, the normalized spectral amplitudes (selected at 200 GHz) are plotted as a function of the distance along the two-component system for both the optimized surfactant and a mismatched surfactant with *n*-octane. What this data reveals is that there is a discernible difference between the optimized and mismatched surfactant systems that can be observed directly by monitoring the evolution of the system over time. Clearly the optimized surfactant continuously evolves while the mismatched surfactant settles along the immiscible interface, hence the halt in the variation of the spectral amplitude as a function of distance after one hour.

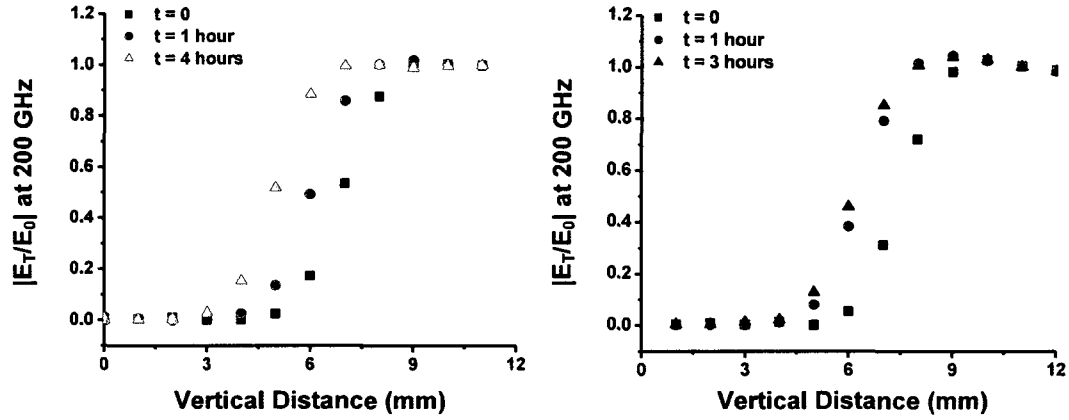

Figure 4-11: Normalized spectral amplitude (selected at 200 GHz) versus distance relative to the mixing interface for three times after mixing. Data collected for optimized cosurfactant (left) and a mismatched surfactant (right) with *n*-octane.

Of greater use is characterizing the approximate interfacial width of the intermediate emulsion layer using the same procedure for estimating the beam diameter.

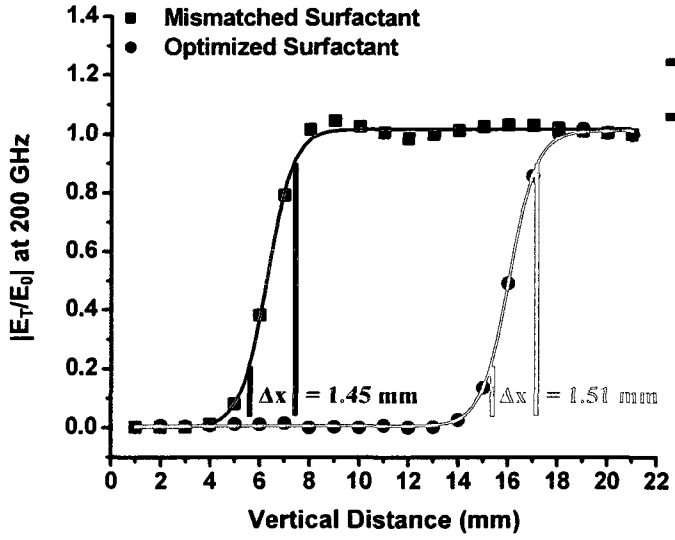

Figure 4-12: Comparison of interfacial width of optimized and mismatched surfactants at t = 1 hour.

t (hours)	d_{Opt}(mm)	d_{Mis}(mm)
0	2.42	2.31
1	2.36	2.26
3	N/A	2.31
4	2.28	N/A

Figure 4-13: Interfacial widths (±0.03 mm) of the optimized and mismatched surfactants at various times.

What this reveals is that there is a quantifiable difference between the two mixtures as the mismatched surfactant segregates along the boundary layer approximately one hour after

mixing while the optimized surfactant continuously evolves. In the sample using the optimized surfactant, the initial interfacial width is the largest as a consequence of the surfactants' ability to efficiently emulsify the octyl chains in the brine solution. However, the interfacial layer starts out at the large width and it quickly equilibrates to a thickness that approaches the interfacial widths of both the mismatched surfactant and water/octane system. That the microemulsion could evolve to an interfacial layer potentially smaller than that in the mismatched surfactant (Figure 4-13) is possible through the preferential intermolecular hydrogen bonding network formed with the octyl chains which acts to wet the surface and minimize the interface between the otherwise immiscible layers. This result is only speculative, though, as the interfacial widths for all the data collected more than one hour after mixing are within the error of the measurement. Additionally, while it is tempting to try and extrapolate stochiometric relationships for the concentrations of the absorbing brine in the non-absorbing *n*-octane from the normalized spectral amplitudes, this approach is unreliable without determining the absorption coefficients of the polar solvent (although it could eventually prove to be accurate).

Ultimately, this experimental setup represents an automated platform that can analyze any multi-component system and the emulsified intermediates between immiscible phases. Although concentrations of the chemical components were not obtained in this initial experiment, this information will be determined with millimeter resolution in subsequent experiments to quantitatively describe the dynamics and components present along miscible and immiscible interfaces.

Chapter 5

Terahertz Spectroscopy of Non-Polar Solids

5.1 Terahertz Vibrational Modes Induced by Crystal Nucleation in *n*-alkanes

Crystal nucleation from a liquid is one of the most thoroughly studied phase transitions with the behavior of *n*-alkanes garnering particular interest due to the presence of distinct features between the liquid-to-crystalline transitions [107, 109, 137-138]. Specifically, the crystallization pathway proceeds via one or more intermediate rotator phases exhibiting long-range order in the molecular orientation and center-of-mass coordinates but disorder in the rotational coordinate along the molecular axis. The rotator phases have been extensively studied due to the crucial role they play in crystal nucleation [105-106, 139]. Additionally, *n*-alkanes exhibit surface *freezing*, where a crystalline monolayer forms at the surface of the liquid, at temperatures above the bulk freezing temperature [140]. This surface frozen layer is believed to act as a nucleation site for growth of the rotator phase from the liquid; however, experimental characterization of this surface-induced heterogeneous phase transition remains elusive [141]. Because alkanes serve as a model system for polymers, surfactants ad biomembranes, the unique aspects of this phase transition have wide implications, and the development of new experimental tools for probing these dynamics are of compelling interest.

To study the freezing transition of *n*-alkanes, we utilized the same THz-TDS setup and temperature-controlled cell used to study liquid *n*-alkanes (Chapter 4). Samples were obtained from a commercial vendor with purities greater than 99.5% and melting points near room temperature ($C_{16}H_{34}$ - $C_{26}H_{54}$) which could then be slowly

cooled at a rate of less than 0.01°C/min to avoid forming amorphous crystals. For such a large variation in carbon chain length (*n* ranging from 16 – 26), the liquid-to-crystalline transition can undergo first or higher order transitions depending on the stability of the rotator phase and dictated by the carbon number. For chain lengths with 22 or fewer carbon atoms, the rotator phase is transient or metastable leading to first order phase behavior (see Figure 5-1):

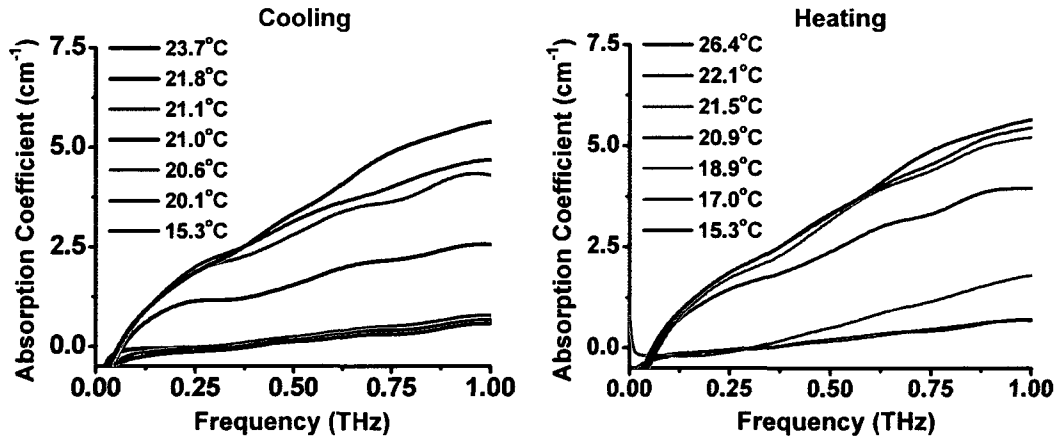

Figure 5-1: Frequency-dependent absorption coefficient of *n*-heptadecane ($C_{17}H_{36}$) as it is both cooled and heated through its melting point (21°C).

Both plots display broad, featureless absorption profiles that increase monotonically with frequency and scale with density indicative of pure scattering phenomena. Further illustration of the first order behavior can be seen in Figure 5-2 where the absorption coefficient is selected at a single frequency and plotted versus temperature to reveal a hysteresis present depending on the direction the melting point is approached from.

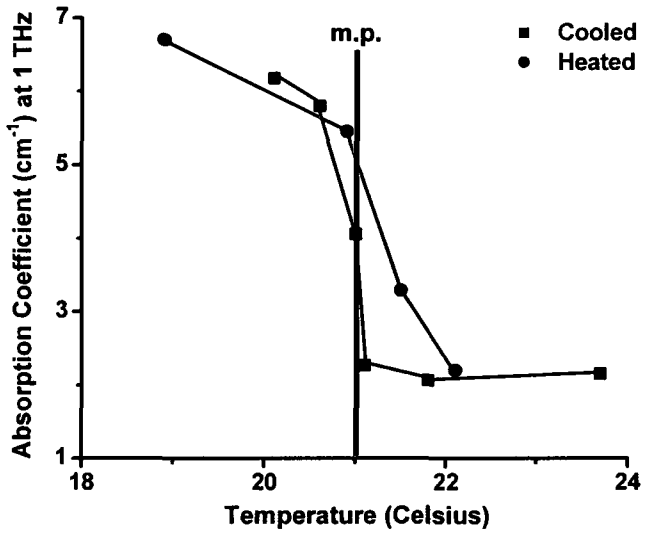

Figure 5-2: Absorption coefficient (selected at 1 THz) vs. temperature for *n*-heptadecane ($C_{17}H_{36}$) illustrating the presence of a hysteresis.

This behavior stands in stark contrast to what is observed in chain lengths with 23 or more carbon atoms which poses fully stable rotator phases and undergo higher order phase transitions. Figure 5-3 depicts the measured absorption spectra for *n*-tetradecane ($C_{24}H_{50}$) in the liquid and rotator phases as well as the liquid-to-rotator transition:

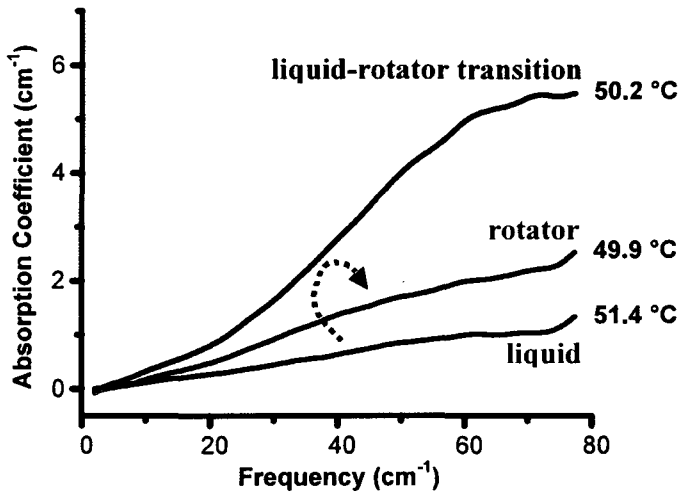

Figure 5-3: Absorption spectra of $C_{24}H_{50}$ at three different temperatures corresponding to the liquid phase (red), liquid-to-rotator transition (black), and the rotator phase (blue).

The absorption is notably larger in the rotator phase than the liquid phase due mostly to scattering from grain boundaries in the polycrystalline samples. However, over a very narrow range at the liquid-to-rotator transition temperature, the absorption is even higher. This enhanced absorption is a signature of the formation of the rotator phase and is not observed upon rapid cooling into an amorphous solid. Similar results are observed in all of the stable rotator phase *n*-alkanes studied (Figure 5-4) and since this enhanced absorption is only observed near the phase transition (within 0.3°C), it seems likely that it is associated with the initial nucleation of the solid. Further cooling of the sample crystallizes it into the rotator phase and removes the excess absorption.

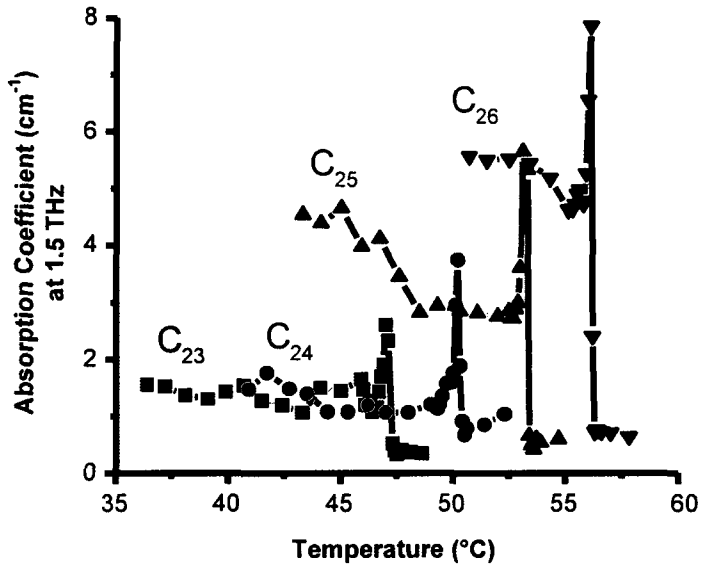

Figure 5-4: Absorption coefficient (at 1.5 THz) vs. temperature for $C_{23}H_{48}$ - $C_{26}H_{54}$.

One possible origin for the absorption feature is light scattering arising from a heterogeneous microstructure formed during nucleation. However, the refractive index of the liquid differs from that of the fully-formed rotator phase by only a few percent,

thus the dielectric contrast is too small to give rise to the observed spectral features (Figure 5-5).

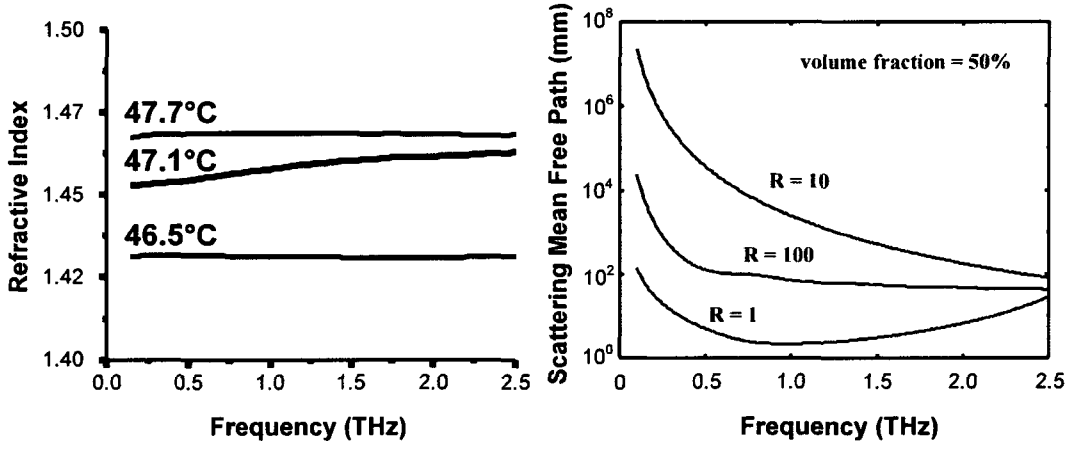

Figure 5-5: Frequency-dependent refractive indices of $C_{23}H_{48}$ at several sample temperatures (left). Calculated scattering mean free path based on Mie scattering from an object with a refractive index of 1.47 embedded in a dielectric host with a refractive index of 1.42 and assuming three different radii occupying 50% of the volume fraction of the medium (right).

If light scattering can be ruled out as the source of the excess absorption, then it must arise from dipole correlations induced in this non-polar material by the liquid-to-rotator transition. To obtain the spectra of the excess absorption, we subtract the absorption spectrum in the rotator phase from that of the transition phase, $\Delta\alpha = \alpha_{L\text{-}R} - \alpha_R$. This is the traditional method used to study collision-induced absorption in various non-polar liquids [142-143] and depicted in Figure 5-6. In the differential spectrum a broad peak is observed below 2.5 THz for all four samples. The solid fits are to a generalized Langevin theory based on the Mori memory function (Chapter 2) for the dipole correlation decay which is also common used in the study of non-polar liquids [57, 63].

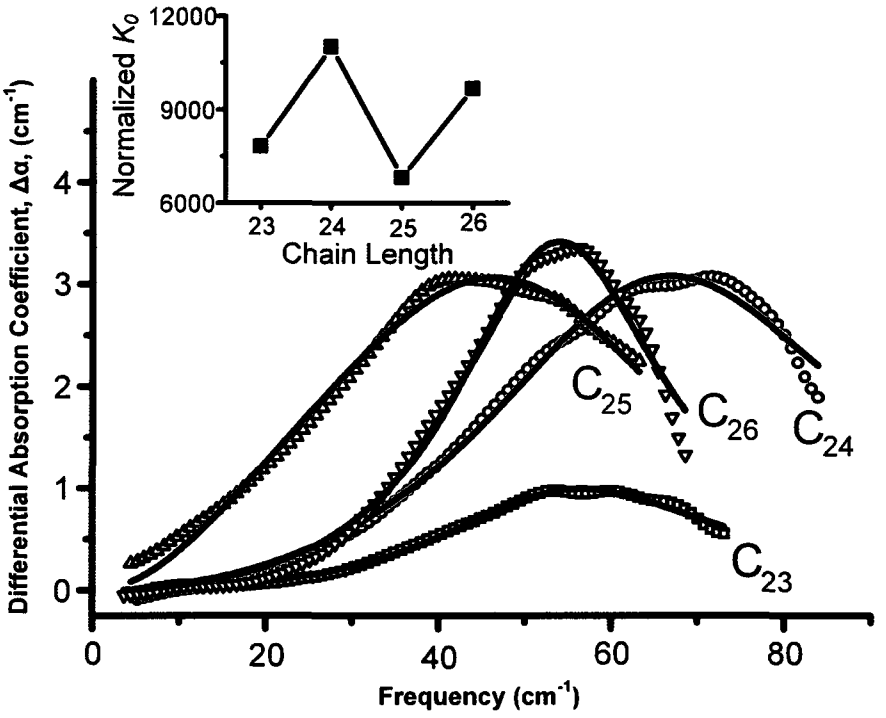

Figure 5-6: Differential absorption spectra for $C_{23}H_{48}$ - $C_{26}H_{54}$. The inset shows the values of the fit parameter K_0, the amplitude of the zeroth-order memory kernel, plotted versus carbon number.

From these fits, parameters associated with the memory function can be extracted, specifically the normalized amplitude of the zeroth-order memory kernel K_0, which are plotted versus chain length in the inset of Figure 5-6. The observed even-odd alteration exhibited by the K_0 values mimics behavior observed in numerous *n*-alkane physical properties [105] and suggests that the end-chain packing of the terminal methyl groups mediates what has to be an induced dipole correlation. Furthermore, this means that the spectral features we observe are a manifestation of short-range intermolecular interactions. The high quality of the fits shown in Figure 5-6 unambiguously indicate that the observed spectral features are a consequence of correlations between induced dipoles in these infrared inactive materials; however, their origins remain unclear.

One possible explanation is based on vibrational modes induced during the nucleation process. Most likely an induced dipole correlation occurs within the small regions of nucleated rotator phase that initially forms near the surface-frozen layer before growing to encompass the entire medium. The effect would relate to the vibrational modes of these nucleated regions and resembles the descriptions of the origin of the Boson peak. This has some precedent and seems reasonable given the striking temperature dependence of the absorption peaks in the differential spectra, especially since it is known that terahertz absorption can be directly correlated with the VDOS in disordered media [141]. Additionally, it has been shown that an enhanced VDOS can result from structuring or heterogeneity on the nanoscale [142-144]. Finally, the idea that *n*-alkanes, upon cooling, may form locally ordered regions with enhanced VDOS has also been proposed previously [145]. Notably, we do not observe any enhanced absorption or signatures of lattice vibrations once the sample is cooled enough so that the rotator phase is fully formed. With the disappearance of mesoscale phase boundaries, one would expect acoustic modes to be largely infrared-inactive, consistent with our observations.

In analyzing the Boson peak in glasses, one can estimate a correlation length scale from the frequency of the peak. We assume that the THz spectra are a direct reflection of the VDOS, so the peak of our measured absorption spectrum corresponds to ν_{max}, the peak of the VDOS [141]. Next, we estimate the vibrational correlation length scale as $D = S(V_s/\nu_{max})$, where S is a factor depending on the shape of the correlated regions, and V_s is the sound velocity [142]. While the sound velocities in *n*-alkanes have not previously been reported for either the crystalline or rotator phases, the room-temperature value for high-density polyethylene ($V_s \sim 2400$ m/s) can be substituted as a reasonable order-of-

magnitude estimate. With this value, and using ν_{max} = 1.6 THz for C_{23} (Figure 5-6) and assuming S = 1, we estimate the correlation length scale to be ~15 Å. This is about half of the inter-layer separation in the C_{23} rotator phase in the lamellar plane and corresponds to roughly four times the nearest-neighbor distance [105]. This estimate suggests that the measured peaks arise from short-range dipolar correlations induced by localized vibrations.

Our observations are consistent with previous studies of low-frequency vibrational modes in alkane crystals. For example, inelastic neutron scattering has been used to study the VDOS in the region below 100 cm^{-1}, for chain lengths less than n = 20 [146]. These results indicate a significant peak in the VDOS near 70 cm^{-1} for even n, and at somewhat lower frequency for odd n. The variation with chain length displayed in Figure 5-6 is consistent with these earlier data and could result from an odd-even alteration in the sound velocity, although the lack of data on the chain-length dependence of V_s makes this speculation difficult to verify.

In conclusion, we present the first evidence for the formation of a Boson peak induced by a first order phase transition. This indicates an enhancement in the vibrational density of states at the phase transition, induced by heterogeneous nucleation. The correlation length scale estimated from the measured spectra suggests that the correlations are relatively short range. More importantly, this result demonstrates a new method for characterizing the dynamics of heterogeneous nucleation in non-polar liquids.

Chapter 6

Discussion and Future Work

6.1 Discussion of Results

We have successfully built a high signal, large bandwidth terahertz time-domain spectrometer along with a temperature-controlled transmission sample cell that were used to characterize the THz optical properties of condensed phase *n*-alkanes. Using this custom experimental equipment we developed numerous novel applications which yielded various unique results. First, we were able to characterize, at 25°C and ambient pressure, all of the *n*-alkanes that are liquid at room temperature to obtain refractive indices that correlate highly to density, surface tension, and viscosity. From these correlations, temperature-dependent calibration curves could be constructed for homologous chains that can predict physical properties for higher chain length linear alkanes, or, more importantly, qualitatively distinguish *n*-alkanes from non-homologous hydrocarbons. Second, we used a commercial THz-TDS, with its rapid scan rate, to image and partially quantify the dynamics across the boundary layer of a two component surfactant/octane system. Using terahertz spectroscopy allows the aqueous and hydrophobic components to be distinguished and can readily discern between optimized and mismatched surfactant and non-polar solvent systems. Performing this experiment with a commercial spectrometer establishes the potential for this technique to be applied to in-situ field work. Finally, using our custom spectrometer and experimental equipment we were able to study the crystallization dynamics of the longer chain length *n*-alkanes ($C_{16}H_{34}$-$C_{26}H_{54}$) with melting points near room temperature. From this work, we observed both first and higher order phase transitions associated with unstable and stable

rotator phase intermediates. In the case of stable rotator phase *n*-alkanes ($n > 23$), the crystal nucleation from the melt induces dipoles between the equilibrium surface frozen monolayer and the bulk liquid that give rise to enhanced absorption spectra. These spectral features were modeled using the generalized Langevin equation which yields a parameter, K_0, related to the moment of inertia of each alkane that alternates when plotted as a function of chain length. The even-odd alteration is observed in numerous physical properties of the *n*-alkanes and is known to be a consequence the terminal methyl group packing in these molecules. This indicates that the origins of these spectral features arise from short-range intermolecular forces and can be attributed to vibrational modes induced in the nucleation process analogous to the Boson peak.

Ultimately, aside from our novel results, all of our experiments demonstrate new applications of THz-TDS that exploit the versatility of terahertz spectroscopy for qualitative and quantitative measurements. Of greater consequence is the extension of THz-TDS to phase transition studies of condensed materials where we have established that it is a new tool capable of characterizing the physics of the crystallization dynamics.

6.2 Future Research Directions

In the future, now that the condensed phase behavior has been characterized for various *n*-alkanes across the liquid and solid states for temperatures below 100°C, there are a number of additional experiments that can be performed. First, given the high correlation between the refractive indices of the *n*-alkanes and the density, surface tension, and viscosity, temperature-dependent measurements can be made to construct calibration curves that would provide accurate methods for calculating physical properties of homologous hydrocarbons. Of greater significance than simply varying the

temperature, though, would be systematically varying the composition of homologous chains which provide a molecular scaffold that can be functionalized with any atomic or molecular group anywhere along the carbon backbone. Given the interesting spectral features observed in the unfunctionalized systems, the addition of polar groups is guaranteed to yield unique absorption profiles which can be used to study the effects specific groups have on dispersion. Immediate progress can be made in regards to these types of studies simply by fixing the internal path length of the single crystal quartz cell to enable quantitative in-situ study of the condensed phase dynamics of numerous alkyl-based systems (polymers, proteins, biomembranes, etc.). Furthermore, the characterization of absorption profiles as a function of molecular group and chain location would provide important feedback in the development of next generation computational methods.

The addition of polar groups to non-absorbing *n*-alkane chains would necessitate new temperature-controlled sample cells with shorter path lengths tailored to higher, unknown, absorption coefficients. Rather than building multiple transmission cells, a single reflection geometry cell would suffice and has already been built (Figure 6-1):

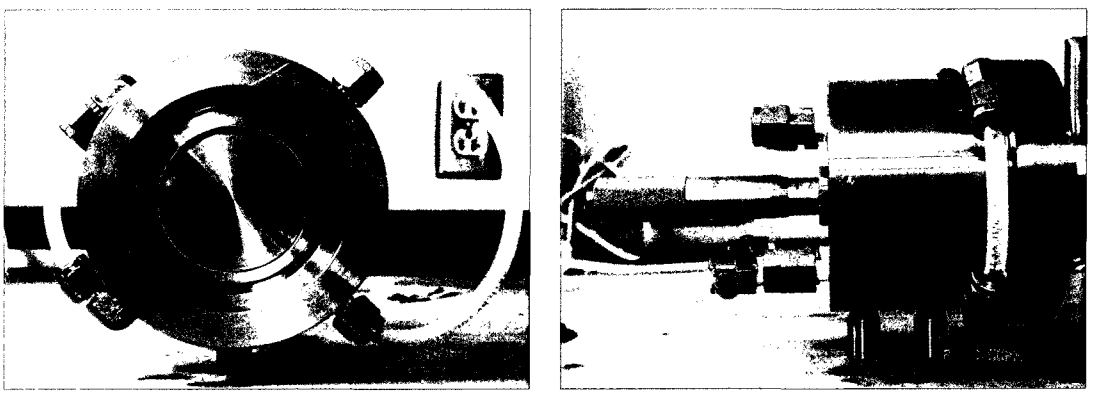

Figure 6-1: Path length and temperature variable reflection sample cell.

This micrometer actuated, reflection cell can be used for multiple path length measurements of any condensed material and adjusted to accommodate the characterization of any material regardless of dipole strength. Utilizing this cell requires a reflection geometry THz-TDS setup and one is currently being built (Figure 6-2):

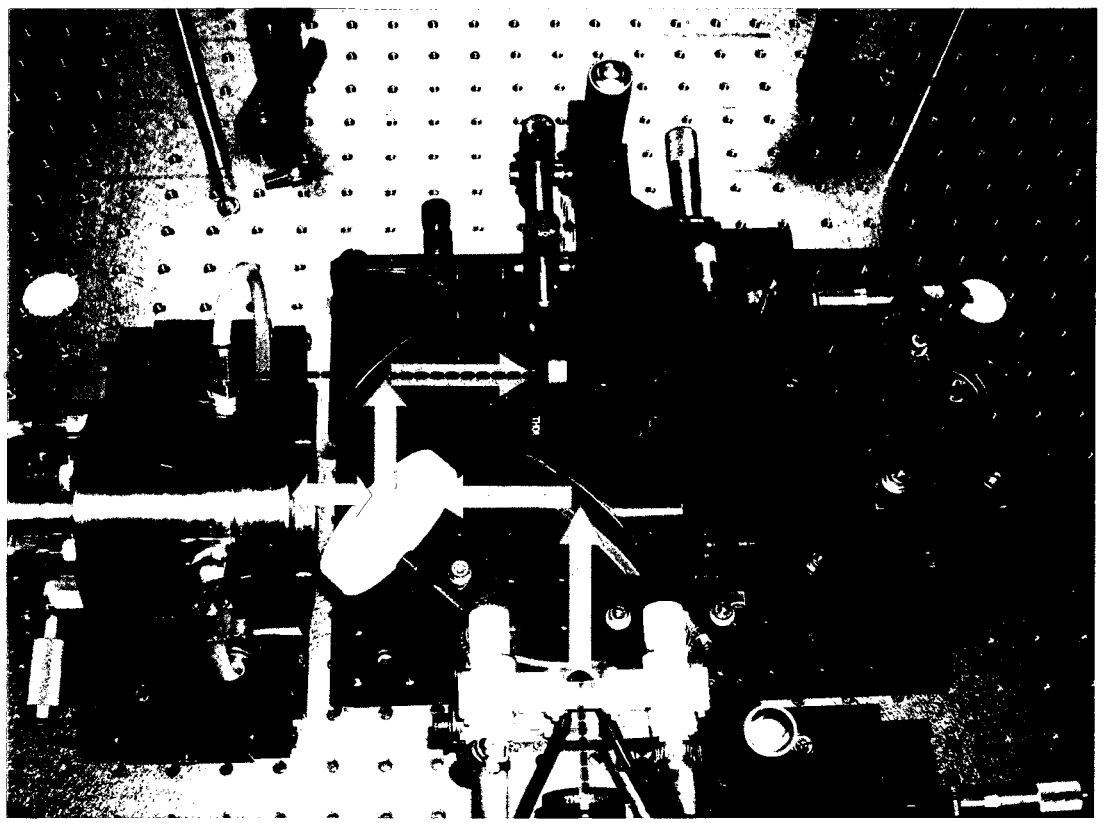

6-2: Reflection geometry THz-TDS setup with path length and temperature variable cell. The THz (green) and probe (red) beam paths are superimposed.

With the new reflection-geometry sample cell and spectrometer, any material can be characterized as a function of temperature to allow further exploration of phase behavior with terahertz time-domain spectroscopy as a new experimental tool for studying condensed matter physics.

Bibliography

1. E. J. Nichols and J. D. Tear, "Joining the infrared and electric wave spectra," Astrophys. J. 61, 17 (1925).

2. D. W. Faries, P. L. Richards, Y. R. Shen, and K. H. Yang, "Tunable far-infrared radiation generated from the difference frequency between two ruby lasers," Phys. Rev. A 3, 2148 (1971).

3. C. V. Shank and E. P. Ippen, "Subpicosecond kilowatt pulses from a mode-locked cw dye laser," Appl. Phys. Lett. 24, 373 (1974).

4. R. L. Fork, B. I. Greene, and C. V. Shank, "Generation of optical pulses shorter than 0.1 psec by colliding pulse mode locking," Appl. Phys. Lett. 38, 671 (1981).

5. P. R. Smith, D. H. Auston, and M. C. Nuss, "Subpicosecond photoconducting dipole antennas," IEEE J. Quant. Elec. 24, 255 (1988).

6. C. Fattinger and D. Grischkowsky, "Terahertz beams," Appl. Phys. Lett. 54, 190 (1989).

7. Q. Wu and X.-C. Zhang, "Free-space electro-optic sampling of terahertz beams," Appl. Phys. Lett. 67, 3523 (1995).

8. D. E. Spence, P. N. Kean, and W. Sibbett, "60-fsec pulse generation from a self-mode-locked Ti:sapphire laser," Opt. Lett. 16, 42 (1991).

9. M. van Exter, Ch. Fattinger, and D. Grischkowsky, "TeraHertz time domain spectroscopy of water vapor," Opt. Lett. 14, 1128 (1989).

10. H. Harde, N. Katzenellenbogen, and D. Grischkowsky, "Terahertz coherent transients from methyl chloride vapor," J. Opt. Soc. Am. B 11, 1018 (1994).

11. J. T. Kindt and C. A. Schmuttenmaer, "Far-infrared dielectric properties of polar liquids probed by femtosecond terahertz pulse spectroscopy," J. Phys. Chem. 100, 10373 (1996)

12. S. R. Keiding, "Dipole correlation functions in liquid benzenes measured with terahertz time domain spectroscopy," J. Phys. Chem. A 101, 5250 (1997).

13. D. S. Venables and C. A. Schmuttenmaer, "Far-infrared spectra and associated dynamics in acetonitrile-water mixtures measured with femtosecond THz pulse spectroscopy," J. Chem. Phys. 108, 1935 (1998).

14. T. I. Jeon, D. Grischkowsky, A. K. Mukherjee, and R. Menon, "Electrical characterization of conducting polypyrrole by THz time-domain spectroscopy," Appl. Phys. Lett. 77, 2452 (2000).

15. C. Zhang, K. S. Lee, X.-C. Zhang, X. Wei, Y. R. Shen, "Optical constants of ice Ih crystal at terahertz frequencies," Appl. Phys. Lett. 79, 491 (2001).

16. M. Schall and P. U. Jepsen, "Freeze-out of difference-phonon modes in ZnTe and its application in detection of THz pulses," Appl. Phys. Lett. 77, 2801 (2000).

17. T. R. Globus, D. L. Woolard, T. Khromova, T. W. Crowe, M. Bykhoskaia, B. L. Gelmont, J. Hesler, A. C. Samuels, "THz-spectroscopy of biological molecules," J. Biol. Phys. 29, 89 (2003).

18. K. Siegrist, C. R. Bucher, I. Mandelbaum, A. R. Hight Walker, R. Balu, S. K. Gregurick, and D. F. Plusquellic, "High-resolution terahertz spectroscopy of crystalline trialanine: extreme sensitivity to β-sheet structure and cocrystallized water," J. Am. Chem. Soc. 128, 5764 (2006).

19. P. U. Jepsen and S. J. Clark, "Precise *ab-initio* prediction of terahertz vibrational modes in crystalline systems," Chem. Phys. Lett. 442, 275 (2007).

20. H. B. Liu, Y. Chen, X.-C. Zhang, "Characterization of anhydrous and hydrated pharmaceutical materials with THz time-domain spectroscopy," J. Pharm.Sci. 96, 927 (2006).

21. D. G. Allis, D. A. Prokhorova, and T. M. Korter, "Solid-state modeling of the terahertz spectrum of the high explosive HMX," J. Phys. Chem. A 110, 1951 (2006).

22. M. R. Leahy-Hoppa, M. J. Fitch, X. Zheng, L. M. Hayden, R. Osiander, "Wideband terahertz spectroscopy of explosives," Chem. Phys. Lett. 434, 227 (2007).

23. P. U. Jepsen, U. Møller, and H. Merbold, "Investigation of aqueous alcohol and sugar solutions with reflection terahertz time-domain spectroscopy," Opt. Express 15, 14717 (2007).

24. R. A. Cheville and D. Grischkowsky, "Far-infrared terahertz time-domain spectroscopy of flames," Opt. Lett. 20, 1646 (1995).

25. M. C. Beard, G. M. Turner, and C. A. Schmuttenmaer, "Subpicosecond carrier dynamics in low-temperature grown GaAs as measured by time-resolved terahertz spectroscopy," J. Appl. Phys. 90, 5915 (2001).

26. F. A. Hegmann, R. R. Tykwinski, K. P. H. Lui, J. E. Bullock, J. E. Anthony, "Picosecond transient photoconductivity in functionalized pentacene molecular crystals probed by terahertz pulse spectroscopy," Phys. Rev. Lett. 89, 227403 (2002).

27. E. Hendry, J. M. Schins, L. P. Candeias, L. D. A. Siebbeles, and M. Bonn, "Efficiency of exciton and charge carrier photogeneration in a semiconducting polymer," Phys. Rev. Lett. 92, 196601 (2004).

28. G. Haran, W. D. Sun, K. Wynne, and R. M. Hochstrasser, "Femtosecond far-infrared pump-probe spectroscopy: A new tool for studying low-frequency vibrational dynamics in molecular condensed phases," Chem. Phys. Lett. 274, 365 (1997)

29. E. Knoesel, M. Bonn, J. Shan, and T. F. Heinz, "Charge transport and carrier dynamics in liquids probed by THz time-domain spectroscopy," Phys. Rev. Lett. 86, 340 (2001).

30. B. B. Hu and M. C. Nuss, "Imaging with terahertz waves," Opt. Lett. 20, 1716 (1995).

31. D. M. Mittleman, M. Gupta, R. Neelamani, R. G. Baranuik, J. V. Rudd, M. Koch, "Recent advances in terahertz imaging," Appl. Phys. B 68, 1085 (1995).

32. D. M. Mittleman, R. H. Jacobsen, and M. C. Nuss, "T-Ray Imaging," IEEE J. Sel. Top. Quant. Elec. 2, 679 (1996).

33. J. F. Federici, B. Schulkin, F. Huang, D. Gary, R. Barat, F. Oliveira, and D. Zimdars, "THz imaging and sensing for security applications – explosives, weapons and drugs," Semicond. Sci. Tech. 20, S266 (2005).

34. R. M. Woodward, V. P. Wallace, D. D. Arnone, E. H. Linfield, and M. Pepper, "Terahertz pulsed imaging of skin cancer in the time and frequency domain," J. Biol. Phys. 29, 257 (2003).

35. P. M. Chaikin and T. C. Lubensky, *Principles of Condensed Matter Physics*, (Cambridge University Press, New York, 1995).

36. G. W. Chantry, *Long-Wave Optics. Vol. 1: Principles*, (Academic Press Inc., London, 1984).

37. Yun-Shik Lee, *Principles of Terahertz Science and Technology*, (Springer US, New York, 2009).

38. D. S. Venables, A. Chiu, and C. A. Schmuttenmaer, "Structure and dynamics on nonaqueous mixtures of dipolar liquids. I. Infrared and far-infrared spectroscopy," J. Chem. Phys. 113, 3243 (2000).

39. M. L. T. Asaki, A. Redondo, T. A. Zawodzinski, and A. J. Taylor, "Dielectric relaxation of electrolyte solutions using terahertz transmission spectroscopy," J. Chem. Phys. 116, 8469 (2002).

40. G. C. Walker, E. Berry, S. W. Smye, N. N. Zinov'ev, A. J. Fitzgerald, R. E. Miles, M. Chamberlain, and M. A. Smith, "Modelling the propagation of terahertz radiation through a tissue simulating phantom," Phys. Med. Biol. 49, 1853 (2004).

41. K. J. Tielrooij, D. Paparo, L. Piatkowski, H. J. Bakker, and M. Bonn, "Dielectric relaxation dynamics of water in model membranes probed by terahertz spectroscopy," Biophys. J. 97, 2484 (2009).

42. B. N. Flanders, R. A. Cheville, D. Grischkowsky, and N. F. Scherer, "Pulsed terahertz transmission spectroscopy of liquid $CHCl_3$, CCl_4, and their mixtures," J. Phys. Chem. 100, 11824 (1996).

43. B. Bagchi and R. Biswas, "Polar and nonpolar solvation dynamics, ion diffusion, and vibrational relaxation: Role of biphasic solvent response in chemical dynamics, "Adv. Chem. Phys. 109, 207 (1999).

44. U. Møller, D. G. Cooke, K. Tanaka, and P. U. Jepsen, "Terahertz reflection spectroscopy of Debye relaxation in polar liquids," J. Opt. Soc. Am. B 26, A113 (2009).

45. P. U. Jepsen and H. Merbold, "Terahertz reflection spectroscopy of aqueous NaCl and LiCl solutions," J. Infrared Millim. Te. 31, 430 (2010).

46. L. Thrane, R. H. Jacobsen, P. U. Jepsen, and S. R. Keiding, "THz reflection spectroscopy of liquid water," Chem. Phys. Lett. 240, 330 (1995).

47. C. Rønne, L. Thrane, P. O. Åstrand, A. Wallqvist, K. V. Mikkelsen, and S. R. Keiding, "Investigation of the temperature dependence of dielectric relaxation in liquid water by THz reflection spectroscopy and molecular dynamics simulation," J. Chem. Phys. 107, 5319 (1997).

48. C. Rønne, P. O. Åstrand, and S. R. Keiding, "THz spectroscopy of liquid H_2O and D_2O," Phys. Rev. Lett. 82, 2888 (1999).

49. A. Beneduci, "Which is the effective time scale of the fast Debye relaxation process in water," J. Mol. Liq. 138, 55 (2008).

50. D. A. Schmidt, Ö. Birer, S. Funker, B. P. Born, R. Gnanasekaran, G. W. Schwaab, D. M. Leitner, and M. Havenith, "Rattling in the cage: Ions as probes of sub-picosecond water network dynamics," J. Am. Chem. Soc. 131, 18512 (2009).

51. W. M. Heston and C. P. Smyth, "Microwave absorption and molecular structure in liquids. 4. The dielectric losses and absolute dielectric constants of some non-polar liquids," J. Am. Chem. Soc. 72, 99 (1950).

52. S. K. Garg, J. E. Bertie, H. Kilp, and C. P. Smyth, "Dielectric relaxation, far-infrared absorption, and intermolecular forces in non-polar liquids," J. Chem. Phys. 49 2551 (1968).

53. U. Stumper. "Dielectric absorption of liquid normal alkanes in the microwave and far-infrared regions," Adv. Mol. Relax. Int. Pr. 7, 189 (1975).

54. W. G. Scaife, J. K. Vij, G. Evans, and M. Evans, "The complex permittivity of six n-alkanes; measurements in the far-infrared," J. Phys. D 15, 1279 (1982).

55. J. K. Vij, "Microwave and far-infra-red dielectric absorption in *n*-alkanes," Nuovo Cimento D 2, 751 (1983).

56. W. Richter and D. Schiel, "Dielectric loss of liquid hydrocarbons in the millimetre and submillimetre wavelength regions," Infrared Phy. 24, 227 (1984).

57. J. E. Pederson and S. R. Keiding, "THz time-domain spectroscopy of nonpolar liquids," IEEE J. Quantum Elec. 28, 2518 (1992).

58. M. Naftaly, A. P. Foulds, R. E. Miles, and A. G. Davies, "Terahertz transmission spectroscopy of nonpolar materials and relationship with composition and properties," Int. J. Infrared Milli. 26, 55 (2005).

59. T. Ikeda, A. Matsushita, M. Tatsuno, Y. Minami, M. Yamaguchi, K. Yamamoto, M. Tani, and M. Hangyo, "Investigation of inflammable liquids by terahertz spectroscopy," Appl. Phys. Lett. 87, 034105 (2005).

60. F. M. Al-Douseri, Y. Chen, and X.-C. Zhang, "THz wave sensing for petroleum industrial applications," Int. J. Infrared Milli. 27, 481 (206).

61. G. W. Chantry, *Long-Wave Optics. Vol. 2: Applications*, (Academic Press Inc., London, 1984).

62. J. P. Poley, "Microwave dispersion of some polar liquids," Appl. Sci. Res. 4, 331 (1955).

63. G. J. Davies and M. Evans, "Use of generalized Langevin theory to describe far infrared absorptions in non-dipolar liquids," J. Chem. Soc. Farad. T 2 72, 1194 (1976).

64. M. Schall, M. Walther, and P. U. Jepsen, "Fundamental and second-order phonon processes in CdTe and ZnTe," Phys. Rev. B 64, 094301 (2001).

65. X. W. Mi, "Optical absorption spectra and intraband dynamics in terahertz-driven semiconductor superlattice," Chinese Phys. Lett. 21, 2536 (2004).

66. D. Grischkowsky, S. R. Keiding, M. van Exter, and Ch. Fattinger, "Far-infrared time-domain spectroscopy with terahertz beams of dielectrics and semiconductors," J. Opt. Soc. Am. B 7, 2006 (1990).

67. W. Xu and X.-C. Zhang, "Resonant absorption of terahertz electromagnetic waves by heated electrons in AlGaAs/GaAs heterostructures," Appl. Phys. Lett. 68, 3305 (1996).

68. T. I. Jeon and D. Grischkowsky, "Nature of conduction in doped silicon," Phys. Rev. Lett. 78, 1106 (1997).

69. M. C. Nuss and J. Orenstern, "Terahertz time-domain spectrocopy," in *Millimeter and Submillimeter Wave Spectroscopy of Solids*, G. Grüner, ed. (Springer-Verlag, Berlin, 1998).

70. T. I. Jeon, K. J. Kim, C. Kang, S. J. Oh, J. H. Son, K. H. An, D. J. Bae, and Y. H. Lee, "Terahertz conductivity of anisotropic single walled carbon nanotube films," Appl. Phys. Lett. 80, 3403 (2002).

71. V. K. Thorsmolle, B. Wenger, J. Teuscher, C. Bauer, J. E. Moser, "Dynamics of photoinduced interfacial electron transfer and charge transport in dye-sensitized mesoscopic semiconductors," CHIMIA 61, 631 (2007).

72. K. P. H. Lui and F. A. Hegmann, "Fluence- and temperature-dependent studies of carrier dynamics in radiation-damaged silicon-on-sapphire and amorphous silicon," J. Appl. Phys. 93, 9012 (2003).

73. X. Ai, M. C. Beard, K. P. Knutsen, S. E. Shaheen, G. Rumbles, and R. J. Ellingson, "Photoinduced charge carrier generation in a Poly(3-hexylthiolphene) and methanofullerene bulk heterojunction investigated by time-resolved terahertz spectroscopy," J. Phys. Chem. B 110, 25462 (2006).

74. Y. S. Jin, G. J. Kim, and S. G. Jeon, "Terahertz dielectric properties of polymers," J. Korean Phys. Soc. 49, 513 (2006).

75. E. Nguema, V. Vigneras, J. L. Miane, and P. Mounaix, "Dielectric properties of conducting polyaniline films by THz time-domain spectroscopy," Eur. Polym. J. 44, 124 (2008).

76. M. Walther, D. G. Cooke, C. Sherstan, M. Hajar, M. R. Freeman, and F. A. Hegmann, "Terahertz conductivity of thin gold films at the metal-insulator percolation transition," Phys. Rev. B 76, 125408 (2007).

77. A. Pimenov, S. Tachos, T. Rudolf, A. Loidl, A. Schrupp, M. Sing, R. Claessen, and V. A. M. Brabers, "Terahertz conductivity at the Verwey transition in magnetite," Phys. Rev. B 72, 035131 (2005).

78. S. D. Brorson, R. Buhleier, J. O. White, I. E. Trofimov, H. –U. Habermeier, and J. Kuhl, "Kinetic inductance and penetration depth of thin superconducting films measured by THz-pulse spectroscopy," Phys. Rev. B 49, 6185 (1994).

79. M. C. Nuss, K. W. Goossen, J. P. Gordon, P. M. Mankiewich, and M. L. O'Malley, "Terahertz time-domain measurement of the conductivity and superconducting band gap in niobium," J. Appl. Phys. 70, 2238 (1991).

80. P. Gu, M. Tani, S. Kono, K. Sakai, and X.-C. Zhang, "Study of terahertz radiation from InAs and InSb," J. Appl. Phys. 91, 5533 (2002).

81. K. Liu, J. Xu, T. Yuan, and X.-C. Zhang, "Terahertz radiation from InAs induced by carrier diffusion and drift," Phys. Rev. B 73, 155330 (2006).

82. H. Zhan, J. Deibel, J. Laib, C. Sun, J. Kono, D. M. Mittleman, and H. Munekata, "Temperature dependence of terahertz emission from InMnAs," Appl. Phys. Lett. 90, 012103 (2007).

83. C. Soci and D. Moses, "Terahertz generation from poly(*p*-phenylene vinylene) photoconductive antenna," Synthetic Met. 139, 815 (2003).

84. E. Hendry, M. Koeberg, J. M. Schins, L. D. A. Siebbeles, and M. Bonn, "Ultrafast charge generation in a semiconducting polymer studied with THz emission spectroscopy," Phys. Rev. B 70, 033202 (2004).

85. M. Brucherseifer, M. Nagel, P. H. Bolivar, H. Kurz, A. Bosserhoff, and R. Büttner, "Label-free probing of the binding state of DNA by time-domain terahertz sensing," Appl. Phys. Lett. 77, 4049 (2000).

86. A. G. Markelz, A. Roitberg, and E. J. Heilweil, "Pulsed terahertz spectroscopy of DNA, bovine serum albumin and collagen between 0.1 and 2.0 THz," Chem. Phys. Lett. 320, 42 (2000).

87. J. Nishizawa, K. Suto, T. Sasaki, T. Tanabe, and T. Kimura, "Spectral measurement of terahertz vibrations of biomolecules using GaP terahertz-wave generator with automatic scanning control," J. Phys. D 36, 2958 (2003).

88. M. Walther, B. M. Fischer, and P. U. Jepsen, "Noncovalent intermolecular forces in polycrystalline and amorphous saccharides in the far infrared," Chem. Phys. 288, 261 (2003).

89. T. M. Korter, R. Balu, M. B. Campbell, M. C. Beard, S. K. Gregurick, and E. J. Heilweil, "Terahertz spectroscopy of solid serine and cysteine," Chem. Phys. Lett. 418, 65 (2006).

90. M. R. Kutteruf, C. M. Brown, L. K. Iwaki, M. B. Campbell, T. M. Korter, E. J. Heilweil, "Terahertz spectroscopy of short-chain polypeptides," Chem. Phys. Lett. 375, 337 (203).

91. Y. C. Shen, T. Lo, P. F. Taday, B. E. Cole, W. R. Tribe, and M. C. Kemp, "Detection and identification of explosives using terahertz pulsed spectroscopic imaging," Appl. Phys. Lett. 86, 241116 (2005).

92. K. Kawase, Y. Ogawa, Y. Watanabe, "Non-destructive terahertz imaging of illicit drugs using spectral fingerprints," Opt. Express 11, 2549 (2003).

93. J. H. Sun, J. L. Shen, L. S. Liang, X. Y. Xu, H. B. Liu, and C. L. Zhang, "Experimental investigation on terahertz spectra of amphetamine type stimulants," Chin. Phys. Lett. 22, 3176 (2005).

94. M. Walther, P. Plochocka, B. Fischer, H. Helm, and P. U. Jepsen, "Collective vibrational modes in biological molecules investigated by terahertz time-domain spectroscopy," Biopolymers 67, 310 (2002).

95. N. Laman, S. S. Harsha, and D. Grischkowsky, "Narrow-line waveguide terahertz time-domain spectroscopy of aspirin and aspirin precursors," Appl. Spectrosc. 62, 319 (2008).

96. C. J. Strachan, P. F. Taday, D. A. Newnham, K. C. Gordon, J. A. Zeitler, M. Pepper, and T. Rades, "Using terahertz pulsed spectroscopy to quantify pharmaceutical polymorphism and crystallinity," J. Pharm. Sci. 94, 837 (2005).

97. G. M. Day, J. A. Zeitler, W. Jones, T. Rades, and P. F. Taday, "Understanding the influence of polymorphism on phononspectra: lattice dynamics calculations and terahertz spectroscopy of carbamazepine," J. Phys. Chem. B 110, 447 (2006).

98. S. Ebbinghaus, S. J. Kim, M. Heyden, X. Yu, M. Gruebele, D. M. Leitner, and M. Havenith," Protein sequence- and pH-depedent hydration probed by terahertz spectroscopy," J. Am. Chem. Soc. 130, 2374 (2008).

99. C. Zhang, E. Tarhan, A. K. Ramdas, A. M. Weiner, and S. M. Durbin, "Broadened far-infared absorption spectra for hydrated and dehydrated myoglobin," J. Phys. Chem. B 108, 10077 (2004).

100. Y. Chen, H. Liu, Y. Deng, D. Schauki, M. J. Fitch, R. Osiander, C. Dodson, J. B. Spicer, M. Shur, X.-C. Zhang, "THz spectroscopic investigation of 2,4-dinitrotoluene," Chem. Phys. Lett. 400, 357 (2004).

101. S. Saito, T. M. Inerbaev, H. Mizuseki, N. Igarashi, Y. Kawazoe, "Terahertz vibrational modes of crystalline salicylic acid by numerical model using periodic density functional theory," Jpn. J. Appl. Phys. 1 45, 4170 (2006).

102. Y. Zhang, X.-H. Peng, Y. Chen, J. Chen, A. Curioni, W. Andreoni, S. K. Nayak, X.-C. Zhang, "A first principle study of terahertz (THz) spectra of acephate," Chem. Phys. Lett. 452, 59 (2008).

103. D. M. Small, *The Physical Chemistry of Lipids*, (Plenum Press, New York, 1986).

104. W. F. Seyer, R. F. Patterson, and J. L. Keays, "The density and transition points of the n-paraffin hydrocarbons," J. Am. Chem. Soc. 66, 179 (1944).

105. E. B. Sirota, J. H. E. King, D. M. Singer, and H. H. Shao, "Rotator phases of the normal alkanes: An x-ray scattering study," J. Chem. Phys. 98, 5809 (1993).

106. A. Marbeuf and R. Brown, "Molecular dynamics in n-alkanes: Premelting phenomena and rotator phases," J. Chem. Phys. 124, 054901 (2006).

107. E. B. Sirota and A. B. Herhold, "Transient phase-induced nucleation," Science 283, 529 (1999).

108. R. P. Sear, "Heterogeneous nucleation near metastable first-order bulk and surface phase transitions," Langmuir 18, 7571 (2002).

109. Y. Shinohara, N. Kawasaki, S. Ueno, I. Kobayashi, M. Nakajima, and Y. Amemiya, "Observation of the transient rotator phase of n-hexadecane in emulsified droplets with time-resolved two-dimensional small- and wide-angle x-ray scattering," Phys. Rev. Lett. 94 097801 (2005).

110. B. Q. Xie, G. M. Liu, S. C. Jiang, Y. Zhao, and D. J. Wang, "Crystallization behaviors of n-octadecane in confined space: Crossover of rotator phase from transient to metastable induced by surface freezing," J. Phys. Chem. B 112, 13310 (2008).

111. M. Maroncelli, S. P. Qi, H. L. Strauss, and R. G. Snyder, "Nonplanar conformers and the phase behavior of solid n-alkanes," J. Am. Chem. Soc. 104, 6237 (1982).

112. S. Wietzke, C. Jansen, T. Jung, M. Reuter, B. Baudrit, M. Bastian, S. Chatterjee, and M. Koch, "Terahertz time-domain spectroscopy as a tool to monitor the glass transition in polymers," Opt. Express 17, 19006 (2009).

113. M. C. Beard, G. M. Turner, and C. S. Schmuttenmaer, "Terahertz spectroscopy," J. Phys. Chem. B 106, 7146 (2002).

114. C. S. Schmuttenmaer, "Exploring dynamics in the far-infrared with terahertz spectroscopy," Chem. Rev. 104, 1759 (2004).

115. X. F. Ma and X.-C. Zhang, "Determination of ratios between nonlinear-optical coefficients by using subpicosend optical rectification," J. Opt. Soc. Am. B 10, 1175 (1993).

116. M. Bass, P. A. Franken, J. F. Ward, and G. Weinreich, "Optical rectification," Phys. Rev. Lett. 9, 446 (1962).

117. D. H. Auston, K. P. Cheung, J. A. Valmanis, and D. A. Kleinman, "Cherenkov radiation from femtosecond optical pulses in electro-optic media," Phys. Rev. Lett. 53, 1555 (1984).

118. R. Huber, A. Brodschelm, F. Tauser, and A. Leitenstorfer, "Gerneration and field-resolved detection of femtosecond electromagnetic pulses tunable up to 41 THz," Appl. Phys. Lett. 76, 3191 (2000).

119. G. Chang, C. J. Diven, C. H. Liu, S. L. Williamson, A. Galvanauskas, and T. B. Norris, "Power scalable compact THz system based on an ultrafast Yb-doped fiber amplifier," Opt. Express 14, 7909 (2006).

120. M. C. Hoffmann, K. L. Yeh, J. Hebling, and K. A. Nelson, "Efficient terahertz generation by optical rectification at 1035 nm," Opt. Express 15, 11706 (2007).

121. G. Zhao, R. N. Schouten, N. van der Valk, W. Th. Wenckebach, and P. C. M. Planken, "Design and performance of a THz emission and detection setup based on a semi-insulating GaAs emitter," Rev. Sci. Instrum. 73, 1715 (2002).

122. G.-R. Lin and C.-L. Pan, "Ultrafast response of multi-energy proton-bombarded GaAs photoconductors," Opt. Quant. Electron. 32, 553 (2000).

123. J. V. Rudd and D. M. Mittleman, "Influence of substrate-lens design in terahertz time-domain spectroscopy," J. Opt. Soc. Am. B 19, 319 (2002).

124. S. P. Mickan, R. Shvartsman, J. Munch, X.-C. Zhang, and D. Abbott, "Low noise laser-based T-ray spectroscopy of liquids using double-modulated differential time-domain spectroscopy," J. Opt. B 6, S786 (2004).

125. F. M. Al-Douseri, Y. Chen, and X.-C. Zhang, "THz wave sensing for petroleum industrial applications," Int. J. Infrared Milli. 27, 481 (2006).

126. W. G. S. Scaife and C. G. R. Lyons, "Dielectric permittivity and *pvT* data of some *n*-alkanes," Proc. R. Soc. Lond. A 370, 193 (1980).

127. N. J. Everall, J. M. Chalmers, and P. R. Griffiths, *Vibrational Spectroscopy of Polymers: Principles and Practice*, (John Wiley & Sons Inc., West Sussex, 2007).

128. D. G. Legrand and G. L. Gaines, Jr. "The molecular weight dependence of polymer surface tension," J. Colloid Interf. Sci. 31, 162 (1969).

129. M. R. Riazi and T. A. Al-Sahhaf, "Physical properties of *n*-alkanes and *n*-alkylhydrocarbons: Application to petroleum mixtures," Ind. Eng. Chem. Res. 34, 4145 (1995).

130. J. E. Mark, *Physical Properties of Polymers Handbook*, (AIP Press, New York, 1996).

131. M. J. Rosen, *Surfactants and Interfacial Phenomena*, (John Wiley & Sons, Inc., West Sussex, 1989).

132. B. Jönsson, B. Lindman, K. Holmberg, and B. Kronberg, *Surfactants and polymers in aqueous solutions*, (John Wiley & Sons Inc., West Sussex, 1998).

133. R. Mendelsohn and D. J. Morse, "Vibrational spectroscopic studies of lipid domains in biomembranes and model systems," Chem. Phys. Lipids 96, 141 (1998).

134. S. Adams, A. M. Higgins, and R. A. L. Jones, "Surface-mediated folding and misfolding of proteins at lipid/water interfaces," Langmuir 18, 4854 (2002).

135. G. L. Richmond, "Molecular bonding and interactions at aqueous surfaces as probed by vibrational sum frequency spectroscopy," Chem. Rev. 102, 2693 (2002).

136. J. M. Khosrofian and B. A. Garetz, "Measurement of a gaussian laser beam diameter through the direct inversion of knife-edge data," Appl. Optics 22, 3406 (1983).

137. X. Z. Wu, B. M. Ocko, E. B. Sirota, S. K. Sinha, M. Deutsch, B. H. Cao, and M. W. Kim, "Surface-tension measurements of surface freezing in liquid normal-alkanes," Science 261, 1018 (1993).

138. H. Kraak, E. B. Sirota, and M. Deutsch, "Measurements of homogeneous nucleation in normal-alkanes," J. Chem. Phys. 112, 6873 (2000).

139. A. B. Herhold, J. H. E. King, and E. B. Sirota, "A vanishing nucleation barrier for the *n*-alkane rotator-to-crystal transformation," J. Chem. Phys. 116, 9036 (2002).

140. E. B. Sirota, "Supercooling, nucleation, rotator phases, and surface crystallization of *n*-alkane melts," Langmuir 14, 3133 (1998).

141. T. S. Grigera, V. Martin-Mayor, G. Parisi, and P. Verrocchio, "Phonon interpretation of the 'boson peak' in supercooled liquids," Nature 422, 289 (2003).

142. E. Duval, A. Boukenter, and B. Champagnon, "Vibration eigenmodes and size of microcrystallites in glass: Observation by very-low-frequency Raman scattering," Phys. Rev. Lett. 56, 2052 (1986).

143. J. Boyd, A. Briskman, V. Colvin, and D. Mittleman, "Direct observation of terahertz surface modes in nanometer-sized liquid water pools," Phys. Rev. Lett. 87, 147401 (2001).

144. X. Zhang, R. S. Bandhu, R. Sooryakumar, and B. T. Jonker, "High-frequency standing longitudinal acoustic resonances in supported thin films," Phys. Rev. B 67, 075407 (2003).

145. L. Brambilla and G. Zerbi, "Local order in liquid *n*-alkanes: Evidence from Raman spectroscopic study," Macromol. 38, 3327 (2005).

146. J. Tomkinson, S. F. Parker, D. A. Braden, and B. S. Hudson, "Inelastic neutron Scattering spectra of the transverse acoustic modes of the normal alkanes," Phys. Chem. Chem. Phys. 4, 716 (2002).

Appendix

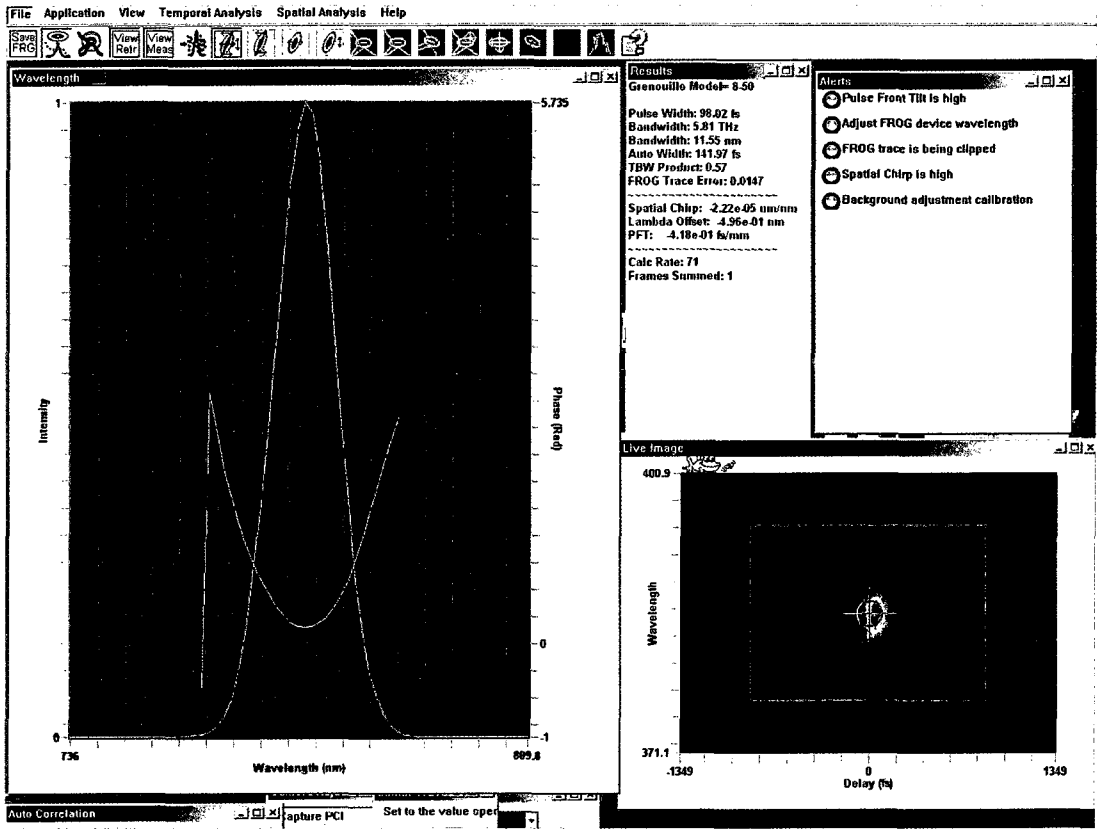

Figure A-1: Frequency Resolved Optical Gating (FROG) trace of the Ti:Sapphire output pulse with a 98 fs chirped output pulse width.

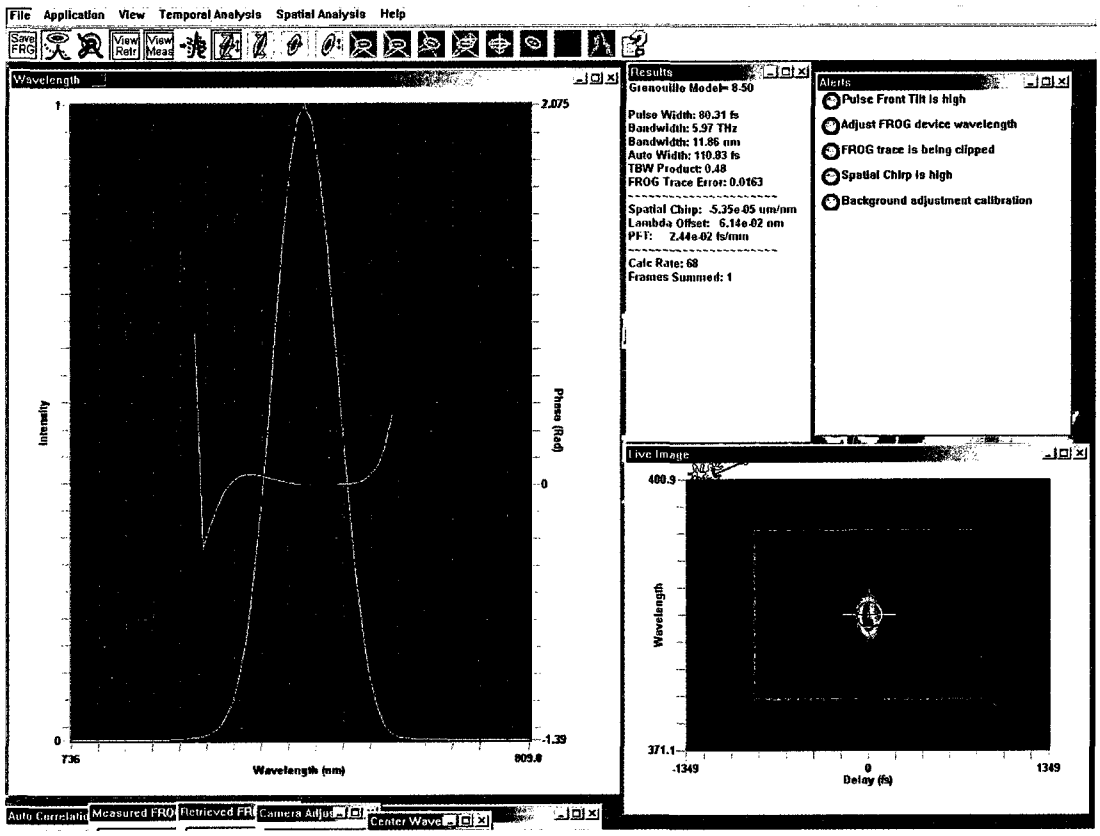

Figure A-2: FROG trace of dispersion compensated Ti:Sapphire pulse with an 80 fs pulse width.

MATLAB code for calculating the absorption coefficient, α(ω), and refractive index, n(ω), for all the single path length measurements using the empty cell as a reference.

```
% LiquidSinglePathLengthAnalysis.m
%
% Designed for input of time-domain signals.
%
% Time Domain x-axis: time
% Freq Domain x-axis: freq
% Time Domain references: signalref
% Time Domain signals: signal
% FFT Amplitudes: ampref and amplitude
% FFT Phases: pharef and phase
% Phase Difference: phasediff
% Index of Refraction: n_mat
% Absorption Coefficient: alpha
% Maximum Abs Coeff: alphamax

clear all
 % Read in the Time-Domain Signals and References
data1=dlmread('hexadecane_55.5C(60C)repeat_purgedalltogether.txt','\t');
data2=dlmread('emptycell_hexadecane_19.9C(20C)_purgedalltogether.txt','\t');

data1zeroed=data1(:,2);
data2zeroed=data2(:,2);

% Average value of floor in Time-Domain Signals
timedomainfloordata1zeroed = find(data1(:,1)<4.0&data1(:,1)>1.0);
timedomainfloordata2zeroed = find(data2(:,1)<4.0&data2(:,1)>1.0);

for a = 1:1
data1zeroedfloor(a) = mean(data1zeroed(timedomainfloordata1zeroed,a));
end

for a = 1:1
data2zeroedfloor(a) = mean(data2zeroed(timedomainfloordata2zeroed,a));
end

% Floor offset correction
data1zeroed=data1zeroed-data1zeroedfloor;
data2zeroed=data2zeroed-data2zeroedfloor;

signal=data1zeroed;
signalref=data2zeroed;

% %# of data points
```

```
n= size(data1,1);

[x,y]=size(signal);

samples=15;

%number of samples
nfft=2^samples;

freq=(0:(nfft-1))/(nfft*(data1(2,1)-data1(1,1)));

N=length(data1(:,1));
deltaT= data1(2,1)- data1(1,1);

% apply time domain trapezoidal window to the data
for jj=1:1
  z=signal(:,jj);
  % find the array index corresponding to the peak of the signal
  minz=find(z==min(z));
  % this next if-then is required since some waveforms have 2 identical minimum
     points, so the "find" function returns a two-by-one array instead of an integer:
  if length(minz)>1
    minz=minz(1);
  end
  % this next if-then checks to see if the peak of the signal is within 6 ps of either the
     beginning or the end of the array:
  if minz*deltaT<6|minz*deltaT>(N*deltaT-6)
    disp(strcat('error',num2str(whichliquid*10+jj)))
    pause
  end
  % here we find the indices corresponding to points that are 6 ps before and 6 ps
     after the peak:
  tmin=minz-round(6/deltaT);
  tmax=minz+round(6/deltaT);
  % now, generate the window function:
  winfunc=zeros(N,1);
  winfunc(tmin:tmax)=windowdan(tmax-tmin+1,'trapezoid',round(4/deltaT));
  % window the signal:
  signal(:,jj)=signal(:,jj).*winfunc;
end

for jj=1:1
  z=signalref(:,jj);
  minz=find(z==min(z));
  if length(minz)>1
    minz=minz(1);
```

```
  end
  if minz*deltaT<6|minz*deltaT>(N*deltaT-6)
    disp(strcat('error',num2str(whichliquid*10+jj)))
    pause
  end
  tmin=minz-round(6/deltaT);
  tmax=minz+round(6/deltaT);
  winfunc=zeros(N,1);
  winfunc(tmin:tmax)=windowdan(tmax-tmin+1,'trapezoid',round(4/deltaT));
  signalref(:,jj)=signalref(:,jj).*winfunc;
end

%fft for signal
for a = 1:1
J1=fft(signal,nfft);
amplitude(:,a)=abs(J1);
phase(:,a)=unwrap(angle(J1));
end

%fft for signalref
for a = 1:1
Jref=fft(signalref,nfft);
ampref(:,a)=abs(Jref);
pharef(:,a)=unwrap(angle(Jref));
end

maxfreq=5;

%average value of noise
noiseindex = find(freq<5&freq>4.5);
for a = 1:1
floor(a) = mean(ampref(noiseindex,a));
end

%Dynamic Range

DR = ampref/floor;

[row, col] = size(freq');

%Thickness matrix definition (in mm)
x(1:row, 1) = 4.40;

%Path length in cm
xmetric = x / 10;
```

```
%Alphamax

for b = 1:nfft
alphamax(b) = 2*((log(DR(b,1))/(xmetric(b))));
end

for a = 1:1
pharef(:, a) = pharef(:,1);
end

%Correction for multiple of 2-pi offset
freqindex=find(freq>0.1&freq<0.5);

for a=1:1
   correctionphase = polyfit(freq(freqindex)',phase(freqindex,a),1);
   correctionpharef = polyfit(freq(freqindex)',pharef(freqindex,a),1);
   corrphase=round(correctionphase(2)/(2*pi));
   corrpharef=round(correctionpharef(2)/(2*pi));
   corrnphase(1:(nfft), a) = corrphase;
   corrnpharef(1:(nfft), a) = corrpharef;
end

pf = phase - 2*pi*corrnphase;
pf = pf - 0*2*pi;
prf = pharef - 2*pi*corrnpharef;

phasediff = pf-prf;

for a=1:1
omega(:, a) = freq'*1e12*2*pi;
end

omegaT = omega.* xmetric;

n_mat = 1 - ((phasediff ./ omegaT) * 3e10);

Ampratio = amplitude ./ ampref;
n_quartz = 2.10;
n_air = 1.0;

for b=1:nfft
a=log((n_air.*((n_mat(b,1) + n_quartz)^2))./(n_mat(b,1).*((n_air +
n_quartz)^2)).*(Ampratio));
alpha = ((2*(-a))./xmetric);
end
```

```
plot(freq, n_mat)
axis([0 5 1.3 1.6])

figure
plot(freq, alpha, freq, alphamax)
axis([0 5 -1 3])

F=freq;
Frequency=F';
N=n_mat;
A=alpha;

dlmwrite('Freq_hexadecane_55.5C(60C).txt',Frequency(1:5:end), 'newline','pc')
dlmwrite('Time_hexadecane_55.5C(60C).txt', data1(:,1), 'newline', 'pc')
dlmwrite('n_mat_hexadecane_55.5C(60C).txt', N(1:5:end), 'newline', 'pc')
dlmwrite('alpha_hexadecane_55.5C(60C).txt', A(1:5:end), 'newline', 'pc')
dlmwrite('waveform_reference_hexadecane.txt', data2zeroed, 'newline', 'pc')
dlmwrite('waveform_hexadecane_55.5C(60C).txt', data1zeroed, 'newline', 'pc')
dlmwrite('windowedwaveform_reference_hexadecane.txt', signalref, 'newline', 'pc')
dlmwrite('windowedwaveform_hexadecane_55.5C(60C).txt', signal, 'newline', 'pc')
dlmwrite('FFT_hexadecane_55.5C(60C).txt', amplitude(1:5:end), 'newline', 'pc')
dlmwrite('FFT_reference_hexadecane.txt', ampref(1:5:end), 'newline', 'pc')
dlmwrite('alphamax_reference_hexadecane.txt', alphamax(1:5:end)', 'newline', 'pc')
```

MATLAB code for calculating the moment of inertia for *n*-tricosane (and can be generalized to all *n*-alkanes).

```
% This program calculates the Moment of Inertia for n-tricosane

mC=12                   % in amu
mH=1.007825             %  "  "
mT=48*mH+23*mC          %  "  "
rCC=1.53                % in angstroms (A)
rCH=1.09                %  "    "
aCC=112.00
aHH=109.50

% I begin by choosing the origin to be at the first terminal carbon atom.
% Since the carbon backbone is planar, there is no z component for any of
% the carbon atoms in the molecule.  Only the hydrogen atoms will have x,y,
% & z components.

xC1=0
yC1=0
zC1=0

xC1H1=-rCH*sin(((aCC/2)*pi)/180)
yC1H1=rCH*cos(((aCC/2)*pi)/180)
zC1H1=0

xC1H2=0
yC1H2=-rCH*cos(((aHH/2)*pi)/180)
zC1H2=rCH*sin(((aHH/2)*pi)/180)

xC1H3=0
yC1H3=-rCH*cos(((aHH/2)*pi)/180)
zC1H3=-rCH*sin(((aHH/2)*pi)/180)

xC2=rCC*sin(((aCC/2)*pi)/180)
yC2=rCC*cos(((aCC/2)*pi)/180)
zC2=0

xC2H1=xC2
yC2H1=rCC*cos(((aCC/2)*pi)/180)+(rCH*sin(((90-aHH/2)*pi)/180))
zC2H1=rCH*cos(((90-aHH/2)*pi)/180)

xC2H2=xC2
yC2H2=rCC*cos(((aCC/2)*pi)/180)+(rCH*sin(((90-aHH/2)*pi)/180))
zC2H2=-rCH*cos(((90-aHH/2)*pi)/180)
```

```
xC3=xC2+rCC*sin(((aCC/2)*pi)/180)
yC3=0
zC3=0

xC3H1=xC3
yC3H1=-rCH*cos(((aHH/2)*pi)/180)
zC3H1=rCH*sin(((aHH/2)*pi)/180)

xC3H2=xC3
yC3H2=-rCH*cos(((aHH/2)*pi)/180)
zC3H2=-rCH*sin(((aHH/2)*pi)/180)

xC4=xC3+rCC*sin(((aCC/2)*pi)/180)
yC4=rCC*cos(((aCC/2)*pi)/180)
zC4=0

xC4H1=xC4
yC4H1=rCC*cos(((aCC/2)*pi)/180)+(rCH*sin(((90-aHH/2)*pi)/180))
zC4H1=rCH*cos(((90-aHH/2)*pi)/180)

xC4H2=xC4
yC4H2=rCC*cos(((aCC/2)*pi)/180)+(rCH*sin(((90-aHH/2)*pi)/180))
zC4H2=-rCH*cos(((90-aHH/2)*pi)/180)

xC5=xC4+rCC*sin(((aCC/2)*pi)/180)
yC5=0
zC5=0

xC5H1=xC5
yC5H1=-rCH*cos(((aCC/2)*pi)/180)
zC5H1=rCH*sin(((aHH/2)*pi)/180)

xC5H2=xC5
yC5H2=-rCH*cos(((aHH/2)*pi)/180)
zC5H2=-rCH*sin(((aHH/2)*pi)/180)

xC6=xC5+rCC*sin(((aCC/2)*pi)/180)
yC6=rCC*cos(((aCC/2)*pi)/180)
zC6=0

xC6H1=xC6
yC6H1=rCC*cos(((aCC/2)*pi)/180)+(rCH*sin(((90-aHH/2)*pi)/180))
zC6H1=rCH*cos(((90-aHH/2)*pi)/180)

xC6H2=xC6
yC6H2=rCC*cos(((aCC/2)*pi)/180)+(rCH*sin(((90-aHH/2)*pi)/180))
```

```
zC6H2=-rCH*cos(((90-aHH/2)*pi)/180)

xC7=xC6+rCC*sin(((aCC/2)*pi)/180)
yC7=0
zC7=0

xC7H1=xC7
yC7H1=-rCH*cos(((aCC/2)*pi)/180)
zC7H1=rCH*sin(((aHH/2)*pi)/180)

xC7H2=xC7
yC7H2=-rCH*cos(((aHH/2)*pi)/180)
zC7H2=-rCH*sin(((aHH/2)*pi)/180)

xC8=xC7+rCC*sin(((aCC/2)*pi)/180)
yC8=rCC*cos(((aCC/2)*pi)/180)
zC8=0

xC8H1=xC8
yC8H1=rCC*cos(((aCC/2)*pi)/180)+(rCH*sin(((90-aHH/2)*pi)/180))
zC8H1=rCH*cos(((90-aHH/2)*pi)/180)

xC8H2=xC8
yC8H2=rCC*cos(((aCC/2)*pi)/180)+(rCH*sin(((90-aHH/2)*pi)/180))
zC8H2=-rCH*cos(((90-aHH/2)*pi)/180)

xC9=xC8+rCC*sin(((aCC/2)*pi)/180)
yC9=0
zC9=0

xC9H1=xC9
yC9H1=-rCH*cos(((aCC/2)*pi)/180)
zC9H1=rCH*sin(((aHH/2)*pi)/180)

xC9H2=xC9
yC9H2=-rCH*cos(((aHH/2)*pi)/180)
zC9H2=-rCH*sin(((aHH/2)*pi)/180)

xC10=xC9+rCC*sin(((aCC/2)*pi)/180)
yC10=rCC*cos(((aCC/2)*pi)/180)
zC10=0

xC10H1=xC10
yC10H1=rCC*cos(((aCC/2)*pi)/180)+(rCH*sin(((90-aHH/2)*pi)/180))
zC10H1=rCH*cos(((90-aHH/2)*pi)/180)
```

```
xC10H2=xC10
yC10H2=rCC*cos(((aCC/2)*pi)/180)+(rCH*sin(((90-aHH/2)*pi)/180))
zC10H2=-rCH*cos(((90-aHH/2)*pi)/180)

xC11=xC10+rCC*sin(((aCC/2)*pi)/180)
yC11=0
zC11=0

xC11H1=xC11
yC11H1=-rCH*cos(((aCC/2)*pi)/180)
zC11H1=rCH*sin(((aHH/2)*pi)/180)

xC11H2=xC11
yC11H2=-rCH*cos(((aHH/2)*pi)/180)
zC11H2=-rCH*sin(((aHH/2)*pi)/180)

xC12=xC11+rCC*sin(((aCC/2)*pi)/180)
yC12=rCC*cos(((aCC/2)*pi)/180)
zC12=0

xC12H1=xC12
yC12H1=rCC*cos(((aCC/2)*pi)/180)+(rCH*sin(((90-aHH/2)*pi)/180))
zC12H1=rCH*cos(((90-aHH/2)*pi)/180)

xC12H2=xC12
yC12H2=rCC*cos(((aCC/2)*pi)/180)+(rCH*sin(((90-aHH/2)*pi)/180))
zC12H2=-rCH*cos(((90-aHH/2)*pi)/180)

xC13=xC12+rCC*sin(((aCC/2)*pi)/180)
yC13=0
zC13=0

xC13H1=xC13
yC13H1=-rCH*cos(((aCC/2)*pi)/180)
zC13H1=rCH*sin(((aHH/2)*pi)/180)

xC13H2=xC13
yC13H2=-rCH*cos(((aHH/2)*pi)/180)
zC13H2=-rCH*sin(((aHH/2)*pi)/180)

xC14=xC13+rCC*sin(((aCC/2)*pi)/180)
yC14=rCC*cos(((aCC/2)*pi)/180)
zC14=0

xC14H1=xC14
yC14H1=rCC*cos(((aCC/2)*pi)/180)+(rCH*sin(((90-aHH/2)*pi)/180))
```

```
zC14H1=rCH*cos(((90-aHH/2)*pi)/180)

xC14H2=xC14
yC14H2=rCC*cos(((aCC/2)*pi)/180)+(rCH*sin(((90-aHH/2)*pi)/180))
zC14H2=-rCH*cos(((90-aHH/2)*pi)/180)

xC15=xC14+rCC*sin(((aCC/2)*pi)/180)
yC15=0
zC15=0

xC15H1=xC15
yC15H1=-rCH*cos(((aCC/2)*pi)/180)
zC15H1=rCH*sin(((aHH/2)*pi)/180)

xC15H2=xC15
yC15H2=-rCH*cos(((aHH/2)*pi)/180)
zC15H2=-rCH*sin(((aHH/2)*pi)/180)

xC16=xC15+rCC*sin(((aCC/2)*pi)/180)
yC16=rCC*cos(((aCC/2)*pi)/180)
zC16=0

xC16H1=xC16
yC16H1=rCC*cos(((aCC/2)*pi)/180)+(rCH*sin(((90-aHH/2)*pi)/180))
zC16H1=rCH*cos(((90-aHH/2)*pi)/180)

xC16H2=xC16
yC16H2=rCC*cos(((aCC/2)*pi)/180)+(rCH*sin(((90-aHH/2)*pi)/180))
zC16H2=-rCH*cos(((90-aHH/2)*pi)/180)

xC17=xC16+rCC*sin(((aCC/2)*pi)/180)
yC17=0
zC17=0

xC17H1=xC17
yC17H1=-rCH*cos(((aCC/2)*pi)/180)
zC17H1=rCH*sin(((aHH/2)*pi)/180)

xC17H2=xC17
yC17H2=-rCH*cos(((aHH/2)*pi)/180)
zC17H2=-rCH*sin(((aHH/2)*pi)/180)

xC18=xC17+rCC*sin(((aCC/2)*pi)/180)
yC18=rCC*cos(((aCC/2)*pi)/180)
zC18=0
```

```
xC18H1=xC18
yC18H1=rCC*cos(((aCC/2)*pi)/180)+(rCH*sin(((90-aHH/2)*pi)/180))
zC18H1=rCH*cos(((90-aHH/2)*pi)/180)

xC18H2=xC18
yC18H2=rCC*cos(((aCC/2)*pi)/180)+(rCH*sin(((90-aHH/2)*pi)/180))
zC18H2=-rCH*cos(((90-aHH/2)*pi)/180)

xC19=xC18+rCC*sin(((aCC/2)*pi)/180)
yC19=0
zC19=0

xC19H1=xC19
yC19H1=-rCH*cos(((aCC/2)*pi)/180)
zC19H1=rCH*sin(((aHH/2)*pi)/180)

xC19H2=xC19
yC19H2=-rCH*cos(((aHH/2)*pi)/180)
zC19H2=-rCH*sin(((aHH/2)*pi)/180)

xC20=xC19+rCC*sin(((aCC/2)*pi)/180)
yC20=rCC*cos(((aCC/2)*pi)/180)
zC20=0

xC20H1=xC20
yC20H1=rCC*cos(((aCC/2)*pi)/180)+(rCH*sin(((90-aHH/2)*pi)/180))
zC20H1=rCH*cos(((90-aHH/2)*pi)/180)

xC20H2=xC20
yC20H2=rCC*cos(((aCC/2)*pi)/180)+(rCH*sin(((90-aHH/2)*pi)/180))
zC20H2=-rCH*cos(((90-aHH/2)*pi)/180)

xC21=xC20+rCC*sin(((aCC/2)*pi)/180)
yC21=0
zC21=0

xC21H1=xC21
yC21H1=-rCH*cos(((aCC/2)*pi)/180)
zC21H1=rCH*sin(((aHH/2)*pi)/180)

xC21H2=xC21
yC21H2=-rCH*cos(((aHH/2)*pi)/180)
zC21H2=-rCH*sin(((aHH/2)*pi)/180)

xC22=xC21+rCC*sin(((aCC/2)*pi)/180)
yC22=rCC*cos(((aCC/2)*pi)/180)
```

```
zC22=0

xC22H1=xC22
yC22H1=rCC*cos(((aCC/2)*pi)/180)+(rCH*sin(((90-aHH/2)*pi)/180))
zC22H1=rCH*cos(((90-aHH/2)*pi)/180)

xC22H2=xC22
yC22H2=rCC*cos(((aCC/2)*pi)/180)+(rCH*sin(((90-aHH/2)*pi)/180))
zC22H2=-rCH*cos(((90-aHH/2)*pi)/180)

xC23=xC22+rCC*sin(((aCC/2)*pi)/180)
yC23=0
zC23=0

xC23H1=xC23+rCH*sin(((aCC/2)*pi)/180)
yC23H1=rCH*cos(((aCC/2)*pi)/180)
zC23H1=0

xC23H2=xC23
yC23H2=-rCH*cos(((aHH/2)*pi)/180)
zC23H2=rCH*sin(((aHH/2)*pi)/180)

xC23H3=xC23
yC23H3=-rCH*cos(((aHH/2)*pi)/180)
zC23H3=-rCH*sin(((aHH/2)*pi)/180)

% Calculate the location of the center of mass

Xcm=(xC1*mC+xC1H1*mH+xC1H2*mH+xC1H3*mH+xC2*mC+xC2H1*mH+xC
2H2*mH+xC3*mC+xC3H1*mH+xC3H2*mH+xC4*mC+xC4H1*mH+xC4H2*mH+
xC5*mC+xC5H1*mH+xC5H2*mH+xC6*mC+xC6H1*mH+xC6H2*mH+xC7*mC+
xC7H1*mH+xC7H2*mH+xC8*mC+xC8H1*mH+xC8H2*mH+xC9*mC+xC9H1*m
H+xC9H2*mH+xC10*mC+xC10H1*mH+xC10H2*mH+xC11*mC+xC11H1*mH+x
C11H2*mH+xC12*mC+xC12H1*mH+xC12H2*mH+xC13*mC+xC13H1*mH+xC1
3H2*mH+xC14*mC+xC14H1*mH+xC14H2*mH+xC15*mC+xC15H1*mH+xC15H
2*mH+xC16*mC+xC16H1*mH+xC16H2*mH+xC17*mC+xC17H1*mH+xC17H2*
mH+xC18*mC+xC18H1*mH+xC18H2*mH+xC19*mC+xC19H1*mH+xC19H2*m
H+xC20*mC+xC20H1*mH+xC20H2*mH+xC21*mC+xC21H1*mH+xC21H2*mH+
xC22*mC+xC22H1*mH+xC22H2*mH+xC23*mC+xC23H1*mH+xC23H2*mH+xC
23H3*mH)/mT

Ycm=(yC1*mC+yC1H1*mH+yC1H2*mH+yC1H3*mH+yC2*mC+yC2H1*mH+yC
2H2*mH+yC3*mC+yC3H1*mH+yC3H2*mH+yC4*mC+yC4H1*mH+yC4H2*mH+
yC5*mC+yC5H1*mH+yC5H2*mH+yC6*mC+yC6H1*mH+yC6H2*mH+yC7*mC+
yC7H1*mH+yC7H2*mH+yC8*mC+yC8H1*mH+yC8H2*mH+yC9*mC+yC9H1*m
H+yC9H2*mH+yC10*mC+yC10H1*mH+yC10H2*mH+yC11*mC+yC11H1*mH+y
```

```
C11H2*mH+yC12*mC+yC12H1*mH+yC12H2*mH+yC13*mC+yC13H1*mH+yC1
3H2*mH+yC14*mC+yC14H1*mH+yC14H2*mH+yC15*mC+yC15H1*mH+yC15H
2*mH+yC16*mC+yC16H1*mH+yC16H2*mH+yC17*mC+yC17H1*mH+yC17H2*
mH+yC18*mC+yC18H1*mH+yC18H2*mH+yC19*mC+yC19H1*mH+yC19H2*m
H+yC20*mC+yC20H1*mH+yC20H2*mH+yC21*mC+yC21H1*mH+yC21H2*mH+
yC22*mC+yC22H1*mH+yC22H2*mH+yC23*mC+yC23H1*mH+yC23H2*mH+yC
23H3*mH)/mT

Zcm=(zC1*mC+zC1H1*mH+zC1H2*mH+zC1H3*mH+zC2*mC+zC2H1*mH+zC2
H2*mH+zC3*mC+zC3H1*mH+zC3H2*mH+zC4*mC+zC4H1*mH+zC4H2*mH+z
C5*mC+zC5H1*mH+zC5H2*mH+zC6*mC+zC6H1*mH+zC6H2*mH+zC7*mC+z
C7H1*mH+zC7H2*mH+zC8*mC+zC8H1*mH+zC8H2*mH+zC9*mC+zC9H1*mH
+zC9H2*mH+zC10*mC+zC10H1*mH+zC10H2*mH+zC11*mC+zC11H1*mH+zC1
1H2*mH+zC12*mC+zC12H1*mH+zC12H2*mH+zC13*mC+zC13H1*mH+zC13H2
*mH+zC14*mC+zC14H1*mH+zC14H2*mH+zC15*mC+zC15H1*mH+zC15H2*m
H+zC16*mC+zC16H1*mH+zC16H2*mH+zC17*mC+zC17H1*mH+zC17H2*mH+z
C18*mC+zC18H1*mH+zC18H2*mH+zC19*mC+zC19H1*mH+zC19H2*mH+zC20
*mC+zC20H1*mH+zC20H2*mH+zC21*mC+zC21H1*mH+zC21H2*mH+zC22*m
C+zC22H1*mH+zC22H2*mH+zC23*mC+zC23H1*mH+zC23H2*mH+zC23H3*m
H)/mT

% Shift the origin to the center of mass

x=[xC1 xC1H1 xC1H2 xC1H3 xC2 xC2H1 xC2H2 xC3 xC3H1 xC3H2 xC4 xC4H1
xC4H2 xC5 xC5H1 xC5H2 xC6 xC6H1 xC6H2 xC7 xC7H1 xC7H2 xC8 xC8H1
xC8H2 xC9 xC9H1 xC9H2 xC10 xC10H1 xC10H2 xC11 xC11H1 xC11H2 xC12
xC12H1 xC12H2 xC13 xC13H1 xC13H2 xC14 xC14H1 xC14H2 xC15 xC15H1
xC15H2 xC16 xC16H1 xC16H2 xC17 xC17H1 xC17H2 xC18 xC18H1 xC18H2 xC19
xC19H1 xC19H2 xC20 xC20H1 xC20H2 xC21 xC21H1 xC21H2 xC22 xC22H1
xC22H2 xC23 xC23H1 xC23H2 xC23H3]

y=[yC1 yC1H1 yC1H2 yC1H3 yC2 yC2H1 yC2H2 yC3 yC3H1 yC3H2 yC4 yC4H1
yC4H2 yC5 yC5H1 yC5H2 yC6 yC6H1 yC6H2 yC7 yC7H1 yC7H2 yC8 yC8H1
yC8H2 yC9 yC9H1 yC9H2 yC10 yC10H1 yC10H2 yC11 yC11H1 yC11H2 yC12
yC12H1 yC12H2 yC13 yC13H1 yC13H2 yC14 yC14H1 yC14H2 yC15 yC15H1
yC15H2 yC16 yC16H1 yC16H2 yC17 yC17H1 yC17H2 yC18 yC18H1 yC18H2 yC19
yC19H1 yC19H2 yC20 yC20H1 yC20H2 yC21 yC21H1 yC21H2 yC22 yC22H1
yC22H2 yC23 yC23H1 yC23H2 yC23H3]

z=[zC1 zC1H1 zC1H2 zC1H3 zC2 zC2H1 zC2H2 zC3 zC3H1 zC3H2 zC4 zC4H1
zC4H2 zC5 zC5H1 zC5H2 zC6 zC6H1 zC6H2 zC7 zC7H1 zC7H2 zC8 zC8H1
zC8H2 zC9 zC9H1 zC9H2 zC10 zC10H1 zC10H2 zC11 zC11H1 zC11H2 zC12
zC12H1 zC12H2 zC13 zC13H1 zC13H2 zC14 zC14H1 zC14H2 zC15 zC15H1
zC15H2 zC16 zC16H1 zC16H2 zC17 zC17H1 zC17H2 zC18 zC18H1 zC18H2 zC19
zC19H1 zC19H2 zC20 zC20H1 zC20H2 zC21 zC21H1 zC21H2 zC22 zC22H1
zC22H2 zC23 zC23H1 zC23H2 zC23H3]
```

```
X=x-ones(1,71)*Xcm
Y=y-ones(1,71)*Ycm
Z=z-ones(1,71)*Zcm

R=[X;Y;Z]
m=[mC mH mH mH mC mH mH mC mH mH mC mH mH mC mH mH mC mH
mH mC mH mH mC mH mH mC mH mH mC mH mH mC mH mH mC mH mH
mC mH mH mC mH mH mC mH mH mC mH mH mC mH mH mC mH mH mC
mH mH mC mH mH mC mH mH mC mH mH mC mH mH mH]
M=diag(m)

%  Compute matrix of products of inertia

MPI=R*M*R'

%  Calculate inertial tensor

I=trace(MPI)*diag(ones(1,3))-MPI

%  Determine principal moments of inertia

Ip=eig(I)

%  Total Inertia

It=Ip(1)+Ip(2)+Ip(3)

%  Total Inertia in kg*m^2

I=It*1.661e-27*1e-20
```